Perylene singlet exciton fission in water solution

Manuel Llansola-Portoles

`manuel.llansola@i2bc.paris-saclay.fr`

Université Paris-Saclay, CEA, CNRS, Institute for Integrative Biology of the Cell (I2BC)
https://orcid.org/0000-0002-8065-9459

Chloe Magne
Université Paris-Saclay, CEA, CNRS, Institute for Integrative Biology of the Cell (I2BC)

Simona Streckaite
Center for Physical Sciences and Technology

Eduardo Domínguez-Ojeda
Insituto de Química, Universidad Nacional Autónoma de México

Andrea Echeverri
Sorbonne Université, CNRS, Laboratoire de Chimie Théorique

Flavio Siro Brigiano
Sorbonne Université, CNRS, Laboratoire de Chimie Théorique

Minh-Huong Ha-Thi
Universite Paris Saclay https://orcid.org/0000-0003-3276-1843

Marius Franckevicius
Center for Physical Sciences and Technology

Vidmantas Jasinskas
Center for Physical Sciences and Technology

Annamaria Quaranta
CEA, iBiTec-S

Andrew Pascal
Université Paris-Saclay, CEA, CNRS, Institute for Integrative Biology of the Cell (I2BC)

THOMAS Pino
CNRS https://orcid.org/0000-0002-1646-7866

Bruno Robert
Institute for Integrative Biology of the Cell (I2BC), CEA, CNRS, Université Paris-Saclay
https://orcid.org/0000-0001-5999-4538

Julia Contreras-García
Sorbonne Université, CNRS, Laboratoire de Chimie Théorique

Daniel Finkelstein-Shapiro
Insituto de Química, Universidad Nacional Autónoma de México

Vidmantas Gulbinas
Department of Molecular Compound Physics, Center for Physical Sciences and Technology

---

Research Article

Keywords: singlet fission, triplet states, triplet excitons, aqueous solution

Posted Date: September 6th, 2024

DOI: https://doi.org/10.21203/rs.3.rs-3414227/v2

Additional Declarations: The authors declare no competing interests.

Preprint

Perylene singlet exciton fission in water solution

Chloe Magne[a], Simona Streckaite[b], Roberto A. Boto[c], Eduardo Domínguez-Ojeda[d], Marina Gromova[e], Andrea Echeverri[f], Flavio Siro Brigiano[f], Minh-Huong Ha-Thi[g], Marius Fanckevičius[b], Vidmantas Jašinskas[b], Annamaria Quaranta[a], Andrew A. Pascal[a], Matthieu Koepf[h], David Casanova[c,i], Thomas Pino[g], Bruno Robert[a], Julia Contreras-García[f], Daniel Finkelstein-Shapiro[d], Vidmantas Gulbinas[b], Manuel J. Llansola-Portoles[a*]

We provide the first direct evidence of singlet fission occurring with water-soluble compounds. We show that perylene-3,4,9,10-tetracarboxylate forms dynamic dimers in aqueous solution, with lifetimes long enough to allow intermolecular processes such as singlet fission. As these are transient dimers rather than stable aggregates, they retain a significant degree of disorder. We performed a comprehensive analysis of such dynamic assemblies using time-resolved absorption and fluorescence spectroscopy, nuclear magnetic resonance spectroscopy, and theoretical modelling, allowing us to observe the characteristic signatures of singlet fission and develop a model to characterize the different species observed. Our findings reveal that structure fluctuations within perylene associations are key in favoring either singlet fission or charge separation. The efficiency of triplet formation is higher than 100%, and the disordered system leads to triplets living in the nanosecond time range.

Introduction

The swift development and implantation of green chemistry is essential in the current environmental emergency[1]. One battlefront for green chemistry is to run chemical reactions driven by solar energy in aqueous media, thus harnessing an unlimited energy supply (solar photons) in a medium that is both abundant and non-hazardous (water). In this framework, the development of multi-electron generation processes to boost the efficiency of photocatalysis in water offers a hypothetical solution that is yet to be exploited. Singlet fission (SF) is a spin-allowed mechanism by which a photo-excited singlet state splits into two distinct spin-triplet excited states [2]. SF was initially described in the 1960s for crystalline anthracene[3] and tetracene[4-6], and it has experienced a surge of interest due to its potential to reach power conversion efficiencies up to 45% [7]. However, a variety of radiative and non-radiative alternative deactivation channels involving ultrafast electronic and vibrational dynamics may compete with SF, limiting these high efficiencies[8-10]. A thorough description of SF mechanisms and the intermediate species involved can be found in several excellent reviews [11-14].

Currently, it is well accepted that the conversion from a singlet exciton (S_1) to independent triplets involves the formation of a correlated triplet-pair state $^1(TT)$, either directly from S_1 or through the mediation of charge transfer (CT) states. Eventually, the system might evolve to form two independent triplets by the loss of electronic, $^1(TT) \rightarrow {}^1(T\cdots T)$, and spin, $^1(T\cdots T) \rightarrow T_1 + T_1$, coherences [13]. However, it is not trivial to determine this apparently simple sequence or even disentangle the role of parallel reactions. This is the case of singlet excimer (^{1}Ex) formation, which has been suggested to act as a promoter for the population of $^1(TT)$, but also as an inhibitor of SF[10-12, 15-18]. Moreover, the spectral signatures of several intermediates are unclear, since transient absorption spectroscopy can produce similar signatures for $^1(TT)$, $^1(T\cdots T)$, and $(T_1 + T_1)$. Even the employment of photon emission to assign $^1(TT)$, trap states, or ^{1}Ex is not unequivocal[10, 17, 19-22]. The identification of the intermediate species becomes especially daunting when the molecular compounds are in solution, that is, with a large degree of configurational freedom, forming weak excitonic couplings, leading to small fluctuations of the electronic levels[16, 23], and consequently to the spectral signatures. Finally, sensitization of triplets is the straightforward method to determine the spectroscopic signature of disentangled triplets and may assist to identify intermediate species[22, 24]. Whereas

[a]*Université Paris-Saclay, CEA, CNRS, Institute for Integrative Biology of the Cell (I2BC), 91198Gif-sur-Yvette, France.*
[b]*Department of Molecular Compound Physics, Center for Physical Sciences and Technology, Saulėtekio Avenue 3, LT-10257 Vilnius, Lithuania*
[c]*Donostia International Physics Center (DIPC), 20018 Donostia, Euskadi, Spain.*
[d]*Insituto de Química, Universidad Nacional Autónoma de México, 04510 Mexico City, Mexico*
[e]*Université Grenoble Alpes, CNRS, CEA, IRIG, MEM, F-38054 Grenoble, France*
[f]*Sorbonne Université, CNRS, Laboratoire de Chimie Théorique, LCT, F. 75005 Paris, France*
[g]*Université Paris-Saclay, CNRS, Institut des Sciences Moléculaires d'Orsay, 91405 Orsay, France.*
[h]*Université Grenoble Alpes, CNRS, CEA, IRIG, Laboratoire de Chimie et Biologie des Métaux, F-38054 Grenoble, France*
[i]*IKERBASQUE, Basque Foundation for Science, 48009 Bilbao, Euskadi, Spain.*

*corresponding author:
Manuel J. LLANSOLA-PORTOLES.
Université Paris-Saclay, CEA, CNRS, Institute for Integrative Biology of the Cell (I2BC), 91198Gif-sur-Yvette, France.
Email: manuel.llansola@i2bc.paris-saclay.fr

there have been many efforts to unravel the details of SF evolution in the solid state or even in non-aqueous solvents[10-12, 15-18], there have been no major advances demonstrating SF in water. Indeed, the current scarcity of studies for SF in aqueous solution is remarkable, with only a few reports involving aqueous suspensions of diketopyrrolopyrrole nanoparticles[25], TIPS-pentacene nanoparticles[26-28], or carotenoid aggregates[29-31]. Moreover, none of these involves molecular systems *in solution*, to create photocatalysts and open new research avenues. In this work, we explore the photophysics of a water-soluble organic system, characterizing the interaction(s) between molecules, the role of disorder, and unequivocally identifying intermediate species. Moreover, we present quantum chemistry simulations to show that the dynamic conformation controls the ability of the system to follow an SF process or charge separation.

Experimental

Preparation of rylene solutions. Perylene-3,4,9,10-tetracarboxylic dianhydride (PTCDA), and Potassium Hydroxide (KOH), were purchased from Sigma-Aldrich and used as received, with a purity of 97 and 90 %, respectively. To prepare perylene solutions, PTCDA was added to 0.5 M KOH in water at room temperature under continuous stirring. This results in hydrolysis of the terminal rings, yielding perylene-3,4,9,10-tetracarboxylic acid (PTC).

UV-Vis Absorption spectra were measured on a Varian Cary E5 Double-beam scanning spectrophotometer (Agilent). Hellma quartz cuvettes of varying pathlengths (10, 4, 2, 1, 0.1, and 0.01 mm) were used to accommodate the large range of PTC concentrations (over 5 orders of magnitude).

1H-NMR. Stock solutions of PTC (90 mM) were prepared in 0.5 M KOH in D_2O (Sigma-Aldrich) just before use. The mixture was sonicated at room temperature for 45 min. All the NMR samples were prepared by diluting the corresponding volume of PTC stock solution with 0.1 M KOH, to obtain the following final concentrations: 1, 5, 10, 25, 40, 45, 50, 60, 70, 75, 80, 85 & 90 mM PTC. All samples were sonicated for 15 min just before taking the NMR spectra. ^{1}H-NMR experiments were acquired at 400 MHz with 32 scans at 25 °C, in a JEOL JNM-ECZ400S spectrometer equipped with a 5 mm probe. The spectra were referenced to the solvent peak at 4.81 ppm, and the pure chemical shifts were reported along with the J coupling splitting. The fits are performed using the most-downfield-shifted resonance.

DOSY experiments. The samples were prepared in deuterated water (D2O, 99.96%-d, Eurisotop) containing 100 µM sodium 3-(trimethylsilyl)propionate (d4-TMSP) as an internal reference. 54 mM, 39 mM, 31 mM, 22.3 mM, 18 mM, 13.3 mM, 9 mM and 4.6 mM solutions of PTC were obtained by dilution of a freshly prepared stock solution of PTC (80 mM, in 0.5M KOH) in 0.1 M KOH. The accurate concentration of each samples were determined by quantitative ^{1}H NMR measurements using sucrose solutions of known concentrations in deuterated water, as standards, and the ERETIC2 module to analyse the data. For the measurements, 600 µL of each solution was used. NMR spectra were recorded on a Bruker Avance spectrometer operating at 500.18 MHz for ^{1}H, equipped with a 5 mm z-gradient BBI probe. All measurements were performed at 298 K. Chemical shifts were reported to the residual HDO signal fixed at 4.81 ppm. In pulsed field gradient ^{1}H NMR mode, the diffusion-filtered spectra were recorded with the standard stimulated echo bipolar pulse gradient sequence (stebpgp1s). The amplitude of the trapezoidal gradient pulses (g) varied from 0.02 to 0.43 T/m. The diffusion coefficients were determined according to the Stejskal–Tanner equation:

$$\frac{I}{I_0} = \exp(-(\gamma_H g\delta)^2 D(\Delta - \frac{\delta}{3} - \frac{\tau}{2}) \quad \text{(eq. 1)}$$

where *I* is the echo intensity at g and I_0 is the echo intensity extrapolated to zero gradient, γ_H is the ^{1}H gyromagnetic ratio, D is the self-diffusion coefficient of the species considered, δ is the gradient pulse duration, Δ is the delay during which the diffusion is observed, and τ is the time interval between the bipolar gradient pulses. The experiments were carried out with δ/2 = 1 ms, Δ = 100 ms, and τ = 0.2 ms. The recycle delay was 7.2 s. Bruker Topspin software package was used for processing all spectra. In each sample, the experimentally-determined diffusion coefficient (D) was corrected by variation of the intrinsic viscosity of the medium, estimated by measuring the diffusion coefficient of the residual solvent signal (HDO). The estimation of the diffusion coefficient was done using HYDROPRO[32] (atomic radius 2.84 A) using the optimized structures for monomer and dimer. From these, the ratio of hydrodynamic radiuses between the two species, $r_{monomer}$ and r_{dimer} was calculated by:

$$\frac{r_{dimer}}{r_{monomer}} = \frac{D_{monomer}}{D_{dimer}} \frac{1}{3} \quad \text{(eq. 2)}$$

Where $D_{monomer}$ and D_{dimer} are the diffusion coefficients of monomer and dimer, respectively.

Nano-to-millisecond transient absorption was performed on an Edinburgh Instruments LP920 Flash Photolysis Spectrometer system, incorporating a Continuum Surelite OPO. The OPO was pumped by a Q-switched Nd:YAG laser operating at 355 nm, having a pulse duration of 5 ns. The LP920 system is equipped with a 450 W pulsed Xenon arc lamp as the probe for the transient absorption measurements. Detection in the LP920 system is performed either via a Czerny-Turner blazed 500-nm monochromator (bandwidth 1-5 nm) coupled with a Hamamatsu R928 photomultiplier tube (kinetics mode), or via a 500-nm-blazed spectrograph (bandwidth 5 nm) coupled with a water-cooled ICCD nanosecond Andor DH720 camera (spectral mode). The samples had an absorbance of ~0.8 at the excitation wavelength and the energy of the laser pulse was ~10 mJ (~15 mJ/cm^2).

Femto–to–nanosecond time-resolved transient absorption. The ultrafast transient absorption (TA) setup was based on an amplified femtosecond laser Pharos 10-600-PP (Light Conversion Ltd., Lithuania), operating at a fundamental wavelength of 1030 nm, with a repetition rate of 50 kHz and a pulse width of ~230 fs. A collinear optical parametric amplifier Orpheus PO15F2L (Light Conversion Ltd., Lithuania) was used to obtain 415 nm wavelength pulses for sample excitation. The measurements were performed at a repetition rate of 4.554 kHz frequency, achieved by using the pulse picker. Excitation was modulated by a mechanical chopper synchronized to the output of the pulse picker. As a probe, we used laser pulses, spectrally broadened by means of continuum generation in a sapphire crystal. The time delay between the pump and probe pulses was varied by an optical delay line based on retroreflector optics mounted on an Aerotech PRO165LM electromechanical translation stage (Aerotech Ltd., UK). The detection equipment consisted of an Andor-Shamrock SR-500i-B1-R spectrometer (Andor Technology, UK) with 150 lines/mm diffraction grating equipped with Andor-Newton DU970 CCD camera (1600 × 200 pixels; Andor Technology Ltd., UK). The reading of the camera was synchronized with the chopper. The data was recorded and processed using home-written software in the LabView programming environment. The changes in absorption (ΔA) were measured as a function of both the wavelength and time delay between pump and probe pulses.

Picosecond time-resolved fluorescence was performed with a streak camera system (Hamamatsu C5680) with synchroscan (M5675) unit coupled to a spectrometer. A femtosecond Yb:KGW oscillator (Light Conversion Ltd., Lithuania) generating 80 fs duration pulses at 1030 nm, which were frequency-tripled to 343 nm (HIRO harmonics generator, Light Conversion Ltd.) at a repetition rate of 76 MHz, was used for the sample excitation. Excitation energy density was attenuated using neutral density filters to about 15 nJ·cm^{-2}. The time resolution of the system was ~8 ps. Signal acquisition time was 1-3 h for each measurement.

Pico-to-nanosecond time-resolved fluorescence was performed with an Edinburgh F920 spectrometer (Edinburgh Instruments, UK). Fluorescence decay kinetics were obtained using time-correlated single photon counting (TCSPC). The excitation source was a picosecond-pulsed diode laser EPL-375 (Edinburgh Instruments, UK) emitting ∼60 ps pulses (5 MHz repetition rate). The temporal resolution of this system was circa 200 ps.

Experimental time-resolved data treatment. Global analysis (sequential, parallel, and target) of time-resolved spectra was performed using commercial CarpetView data analysis software (Light Conversion) with reconvolution with the laser prompt.

Simulations. Optimized molecular structures, vibrational frequencies, and excited states were calculated using Gaussian 16 software[33]. These calculations have been performed with an implicit solvent model (PCM)[34], where a dielectric constant of 78.35 was used to simulate the aqueous solvent. The configurational search for dimers was performed by placing the monomers in the center of cubes of various sizes and allowing them to evolve under annealing conditions, as implemented in the ASCEC program [35, 36]. Following the generation of candidate structures to be minima on the potential energy surface, these structures were subsequently optimised and classified as true minima by evaluation of the eigenvalues of the Hessian matrix at the DFT level of theory, using the M06 functional [37] and the 3-21G basis set[38].

The dynamics of the most stable dimer structure were then simulated by ab initio molecular dynamics (AIMD) in the presence of bulk water at 300K. The liquid phase was modelled with 432 water molecules in a cubic box with an edge length of 24.312 Å (ρH2O ≈ 1.0 g cm3), generated by PACKMOL software[39, 40]. The final model was generated by adding to the simulation box the perylene dimer structure previously optimized by quantum static calculations in the presence of a few explicit molecules and in PCM. The neutrality of the box was ensured by adding four K$^+$ ions into the simulation boxes, in positions close to the perylene carboxylate groups. We adopted Born–Oppenheimer molecular dynamics (BOMD), the PBE[40] approximation of density functional theory in the spin-restricted Kohn–Sham scheme together with Grimme’s D3(BJ) correction for the description of dispersion interactions[41, 42], GTH pseudopotentials[43, 44], combined plane-wave (600 Ry cut-off) and 909879 DZVP-MOLOPT-SR basis sets. Before running the molecular dynamics simulations, the positions of all atoms in the simulation boxes were optimized. The dynamics were run with CP2K/Quickstep code[45] for 30 ps adopting the Nosé–Hoover thermostat[46, 47] to control the average temperature at 300 K in the NVT ensemble. The length of the Nosé–Hoover chain was equal to 3, whereas the time constant of the thermostat was set to 100 fs, with the third-order Yoshida integrator and multiple time step set to 2. Trajectories of 1 ps, with a time step of 0.5 fs, were found to be sufficiently long to reach the target temperature. Only the last 17 ps were considered for analysis. It should be noted that the dimensions of the box lead to a minimal distance between replicas of 12.5 Å along the dynamics and that throughout the entire simulation, the K$^+$ ions remained situated within the first solvation shell of the perylenes. VMD[48] software was used to visualize the MD trajectories and the analysis of the dimer twist angle fluctuations was performed with the Travis package[49, 50].

Electronic couplings have been evaluated using a five-state excitonic model: two low-lying local excited states (LE), which are localized on the monomers, two low-lying CT states, and the ^{1}(TT) state that determines the SF process. To compute electronic couplings, we follow a two-step procedure using the Q-Chem program[51, 52]: we first carry out restricted active space configuration interaction (RASCI)[53, 54] calculations to obtain the low-energy adiabatic states; we then obtain the diabatic state energies and couplings through a diabatization scheme. RASCI calculations have been performed using the Hartree-Fock singlet as the reference configurations, with four electrons and four orbitals in the RAS2 space, including hole and particle excitations, and with the 6-311G(d,p) basis set[55]. Diabatization was performed following the Boys localization scheme[56] for the lowest nineteen excited singlet states.

Results

Steady-state absorption and fluorescence. Perylene-3,4,9,10-tetracarboxylic acid (PTC) is water soluble up to 100 mM. The absorption spectra in the range 0.01–90 mM (Figure 1a, full lines) are devoid of scattering, indicating the absence of large-scale aggregation, and no absorption shifts are observed (which would be indicative of medium/strong excitonic interactions[23, 57, 58]). The vibronic peaks (414, 438, and 466 nm) display a strong concentration dependence in terms of the ratio of intensities between the first and second vibronic bands (R_{abs} = I_{A1}/I_{A2}), and the specific molar absorptivity (ε) (Figure 1b). The decrease in R_{abs} is indicative of H-aggregation, whereas the lack of a blue shift, and the widening of the bands calculated as the difference of FWHM ($\Delta FWHM = 250 \pm 50\ cm^{-1} << \omega_{vib} = 1400\ cm^{-1}$), support the weak nature of the excitonic couplings involved[23, 57, 58]. The hypochromism exhibited by H-aggregates has been associated with the formation of π-π-stacked species[57-59], and rationalized as the distortion, by the electronic excitation of one molecule, of the electronic states of neighboring chromophores[60]. The fluorescence spectra (Figure 1a, dashed lines), with vibronic peaks at 481, 509, and 550 nm, exhibit strong fluorescence quenching at higher concentrations along with an increase in the ratio of the vibronic emission bands ($R_{fluorescence} = I_{F1}/I_{F2}$), both of which are also consistent with the formation of H-aggregates[23].

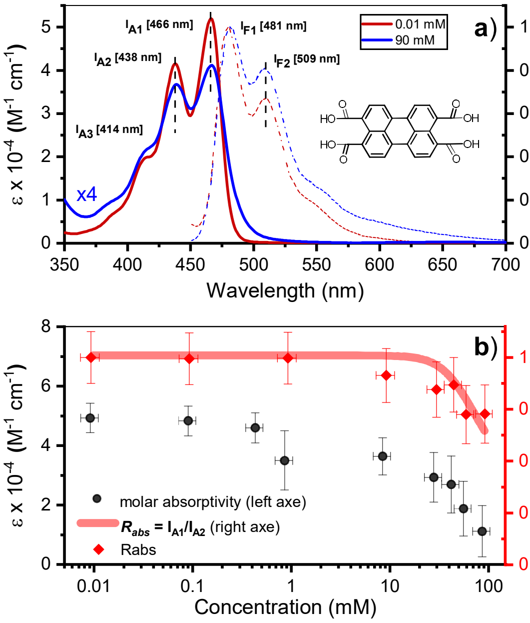

Figure 1. a) Room temperature absorption (solid lines), represented as molar absorption coefficient (ε), and normalized fluorescence (dashed lines) of PTC at 0.01 and 90 mM. The maxima of the vibronic peaks for absorption and fluorescence are marked by vertical black dashed lines and the exact value is described on the side by I_{A1}, I_{A2}, I_{F1}, I_{F2}. **Inset:** Chemical structure of PTC. **b)** Concentration variation of ε at 466 nm (black circles – left y-axis) and R_{abs} (red diamonds – right y-axis). The red line is the fitting of R_{abs} using equation 5 (*vide infra*).

Time resolved fluorescence. The fluorescence decay for two PTC concentrations (10 and 90 mM) has been evaluated by *single photon counting* (SPC) with ca. 200 ps resolution, giving the following decay times: 10 mM (< 200 ps & 4.0 ns), 90 mM (< 200 ps). The fluorescence at higher temporal resolution was measured by streak camera, and fitted by fixing the long components obtained by SPC (see supporting information for 45 mM). The *fluorescence decay associated species* (FDAS) is obtained by multi-exponential parallel fitting and yields the following components for each of the samples: 10 mM (200 ps & 4.0 ns), and 90 mM (20 & 135 ps). This suggests the presence of π-π-stacked species even at low concentrations, which is consistent with the observations by steady state absorption and ^1H-NMR, and probably results from hydrophobic interactions of the PTC core. The absence of any shift in the maxima is consistent with the presence of at least two weak H-aggregated species. It is reasonable to assume that the species decaying in 4.0 ns is monomeric PTC, while the species with shorter lifetimes correspond to the singlet-excited state of dimers/oligomers with different association geometries. We tentatively designate these entities as excimer states (^1Ex), distinguishing them from the monomeric S_1 state.

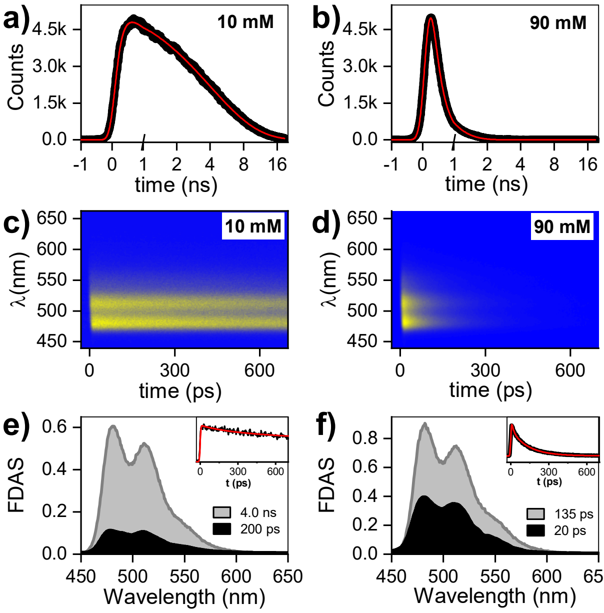

Figure 2. Time-resolved fluorescence – single photon counting (SPC) collected at 510 nm upon 415 nm excitation for **a)** 10 mM, & **b)** 90 mM solution. Time-spectral 2D fluorescence matrix collected by streak camera, fluorescence decay associated spectra (FDAS), and kinetics at 510 nm from **c, e)** 10 mM, & **d, f)** 90 mM solution. The OD was adjusted to less than 0.1 to minimize self-absorption distortion, the excitation was at 343 nm, and the excitation energy was ~15 nJ·cm^{-2}.

Transient absorption spectroscopy in the fs-to-ns window. The evolution of excited states after photoexcitation at 415 nm in Figure 3 shows: dataset, gated spectra, and selected kinetics for 10 and 90 mM PTC solutions. The 10 mM sample exhibits a distinct peak at 740 nm, which can be attributed to excited-state absorption (ESA) resulting from the S_1–S_n transition. Additionally, a negative feature at 515 nm is observed, indicating *stimulated emission* (SE). From 1 to 10 ps, there is negligible change in the spectral features. Subsequently, both the positive and negative features maintain their shape and gradually diminish in intensity at 100 and 1000 ps. This dataset can be fitted to an exponential sequential model with 3 components, attributed to vibrationally-hot monomer/excimer ([hot-S_1/^1Ex]; 1 ps), singlet excimer (^1Ex; 200 ps), and singlet monomer (S_1; 4.0 ns) (see *supplementary information*). It must be noted that for weak excitonic interactions, as in the present case, it has been reported that the S_1–S_n and $^1Ex_1$–^1Ex_n transitions produce indistinguishable electronic signatures[15, 61, 62]. This effect is particularly evident in the work of Marguilles *et al* [62], where the absorption spectrum of the weakly-interacting dyad shows minimal changes compared to the monomer, whereas strongly-interacting dyads exhibit distorted absorption profiles and a distinctive $^1Ex_1$–^1Ex_n transition. The spectral signatures of the S_1–S_n and $^1Ex_1$–^1Ex_n transitions create an isosbestic point at 585 nm (ΔOD = 0). The 90 mM sample at time zero exhibits the 740 nm ESA attributed to S_1–S_n and/or $^1Ex_1$–^1Ex_n transitions, which has a lifetime shorter than 500 ps. Associated to the S_1–S_n and/or $^1Ex_1$–^1Ex_n decay, there is formation of a new species with ESA at 580-610 nm, which was not observed for 10 mM PTC. At the isosbestic point (585 nm), there is a first formation associated to short times (< 100 ps), and a second ESA increase at longer times (100-500 ps). The sequential or parallel model fitting for 90 mM can give an approximation to the overall evolution of the system, but it is not able to produce an accurate physical description (see *supporting information*).

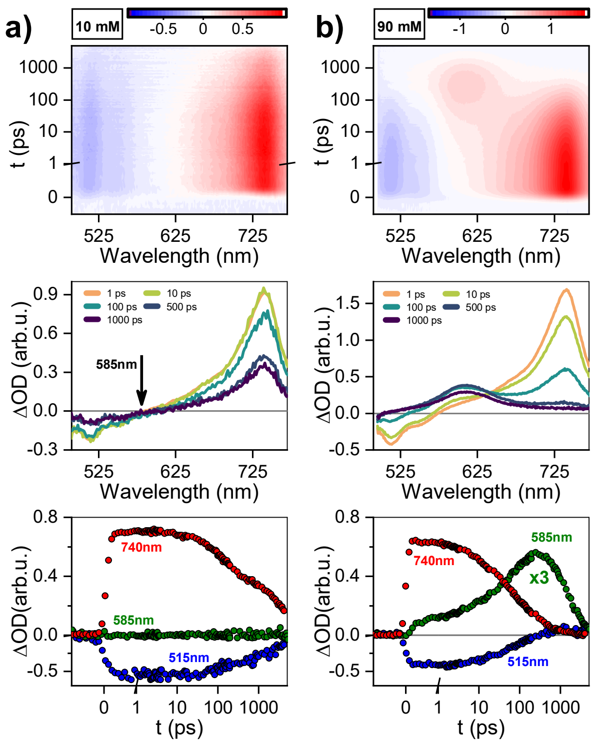

Figure 3. Transient absorption spectra of PTC in the fs-to-ns window: time-spectral map, gated-spectra at 1, 10, 100, 500, and 1000 ps, and kinetics at 515, 585, and 740 nm for **a)** 10 mM, **b)** 90 mM solution. Excitation: 415 nm; power: 100 mW.

To produce a sound model, it is necessary to first identify the unknown species with ESA at 580-610 nm, which unfortunately is subject to controversy. For highly-coupled perylene dimers, an ESA in the 614–625 nm region has been assigned to singlet excimers[63, 64]. However, it is unlikely in our weakly-coupled system, since we have already identified unambiguously the presence of weakly-coupled PTC in our diluted solutions associated to the 740 nm ESA, and we do not observe any associated fluorescence. Papadopoulos *et.al.* attributed this feature to an entangled triplet $^1(TT)$ [24], but the detection of this feature in the nanosecond range rules out the presence of coherent species. A 580-610 nm ESA could be due to perylene cations, but it should have the paired anion signature circa 700-750 nm [24]. The lack of any ESA for long-living species at 740 nm rules out CT in the ns time. However, polar solvents have been reported to favor CT[62], and the perylene anion signature could be obscured due to the overlap with the 740 nm ^{1}Ex-ESA. *A priori*, the triplet species of PDI derivative dimers[24, 65], and crystals [66] are reported to appear in the 600 nm region, making them promising candidates for a preliminary tentative assignment.

Transient absorption spectroscopy in the ns-to-µs window. Figure 4(a,b) shows the dataset and decay-associated spectra for ns-to-µs TA for the 90 mM sample. The dataset is fitted to a mono-exponential decay model, obtaining a component (1.3 µs) with GSB < 500 nm and ESA circa 610 nm. The lack of an ESA peak around 700-750 nm rules out the presence of perylene anions[24] and reinforces the assignment to a triplet state. We designed a sensitization measurement using 1H-Phenalen-1-one as sensitizer[67], which has ultrafast *inter-system crossing* (QY_{ISC} ~ 100%), to make an unequivocal assignment. The sensitization of diluted (0.1 mM) PTC in water yields a transient signature similar to the monomeric triplet reported for perylenes[24], with the main absorption circa 550 nm and a small shoulder circa 600 nm (*see supporting information*). The most concentrated solution (90 mM) was not used since the addition of 1H-Phenalen-1-one surpasses the solubility limit, causing precipitation (*see supporting information*). We therefore performed the sensitization at 45 mM, 1:1 ratio sensitizer/PTC, and in 70/30 (v/v) water/ethanol to maintain solubility. Figure 4(c, d) shows the gated spectra and decay-associated spectra (DAS), yielding two components (24 and 100 µs). The 100 µs DAS is coincident with the monomeric triplet observed for the dilute solution, whereas the 24 µs DAS is similar to the feature observed in the ultra-fast measurements. Hence, the most plausible assignment for this species is the triplet state of perylene aggregates, which we henceforth denote as triplet excimers (^{3}Ex). These triplets are exclusively generated at high concentrations and with remarkable speed, hinting at SF as their underlying formation mechanism.

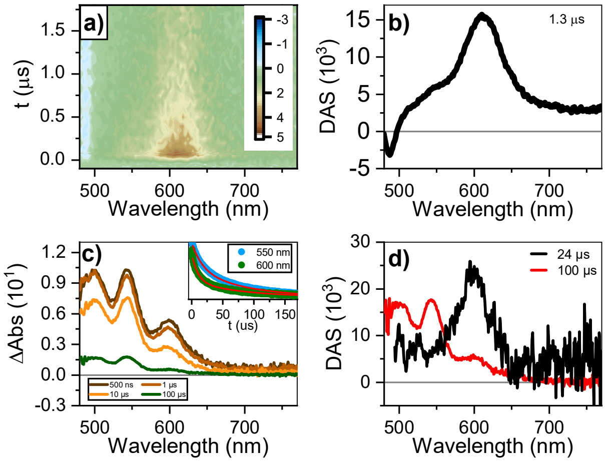

Figure 4. a) Dataset of transient absorption in the ns-to-µs window, and **b)** decay-associated spectra (DAS) for 90 mM solution. **c)** Gated spectra, kinetics (inset), and **d)** DAS of 45 mM PTC in 70/30 (v/v) water/ethanol upon sensitization with 1H-Phenalen-1-one (excitation at 350 nm).

Nuclear Magnetic Resonance. ^{1}H-NMR was used to characterize the interaction between PTC molecules and their resulting structure. We observe two distinct resonances (δ1, δ2) corresponding to dissimilar protons, with a coupling constant of

J=7.9 Hz. Increasing the concentration of PTC causes an upfield shift of both resonances, starting after 10 mM (Figure 5 a, b). The observation of a unique chemical shift for each distinct proton suggests a fast exchange between two or more chemical environments, and not the presence of two or more static species which would appear as two or more chemical shifts per distinct proton, reflecting the different static environments[68]. Perylene dyes have been shown to form indefinite self-assemblies, where oligomers of different lengths coexist in dynamic equilibrium[69, 70]. We fit the data with three different association models (see supporting information for details of the three models):

Model 1: the formation of dimers from PTC monomers.

$$\mathrm{PTC} + \mathrm{PTC} \leftrightarrow (\mathrm{PTC})_2$$

Model 2: the formation of indefinite oligomers.

$$(\mathrm{PTC} + \mathrm{PTC} \leftrightarrow (\mathrm{PTC})_2 + \mathrm{PTC} \leftrightarrow (\mathrm{PTC})_3 \leftrightarrow \ldots)$$

Model 3: a modified dimer model where dimer formation is preceded by complexation with K^+ ions as intermediate steps.

$$\mathrm{PTC} + \mathrm{K} \leftrightarrow \mathrm{PTC\text{-}K} + \mathrm{K} \leftrightarrow \mathrm{PTC\text{-}K_2} + \mathrm{PTC\text{-}K_2} \leftrightarrow (\mathrm{PTC\text{-}K_2})_2$$

In all three cases, in the fast exchange limit, we can fit the observed chemical shift as a weighted average of the equilibrium fraction species i:

$$\delta_{obs} = \sum_{i=1}^{N} f_i \delta_i \qquad \text{(eq. 3)}$$

Where f_i is the fractional population of molecules in species i and δ_i its corresponding chemical shift.

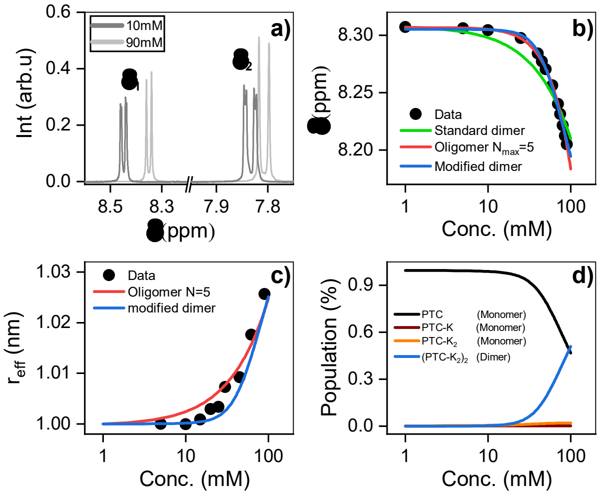

Figure 5. a) 1H NMR chemical shifts showing two distinct environments for the protons (δ_1 & δ_2) (see supporting information). **b)** 1H NMR chemical shift of PTC as a function of concentration, along with the fit to dimers and oligomers with a maximum cutoff of N=5. **c)** Effective radius extracted from DOSY measurements fit with the same models. **d)** Species populations for the modified dimer model.

The simple (standard) dimer model does not reproduce the chemical shifts correctly – the onset of the chemical variation occurs from the lowest concentrations - and the values of the fit do not converge. In particular, the value of the chemical shift for the dimers tends to zero which is unphysical. Both the modified dimer and the oligomer model can explain the observed chemical shift trend; in particular, they both reproduce the onset of the chemical shift variation above 10 mM (Figure 5b). This suggests either that higher size aggregates exist, or that the potassium ions play a role in aggregate formation. The oligomer model however also fails to account for 100% of the species: it requires a maximum cut-off size (N_{max}) of the oligomers, and we find that for cut-off sizes of 5, 10, 15, and 20 there is a significant residual fractional population of 0.075, 0.048, 0.051 and 0.076, respectively. It indicates that the model might not be entirely appropriate for PTC as adding more oligomers does not make the model converge. To unambiguously discriminate between the oligomers and the modified dimer model, we carry out Diffusion Ordered Spectroscopy (DOSY) at several concentrations. Since the system is in the fast exchange regime with respect to the chemical shift differences, we know that the exchange rate has to be much faster than 40 ms (taken as the inverse of the chemical shift difference between monomer and dimer). In this case, the DOSY experiment is also in the fast exchange regime with respect to the diffusion time (100 ms). We then expect to measure an average diffusion coefficient which is equal to the residence-time-weighted average of the diffusion coefficients for monomers and dimers, or oligomers of different sizes.

To minimize systematic errors, we measure the increase in the hydrodynamic radius of the aggregates as:

$$q = \frac{r_{aggregate}}{r_{monomer}} = \sqrt[3]{\frac{D_{monomer}}{D_{HOD}} \frac{D_{HOD}}{D_{aggregate}}} \qquad \text{(eq. 4)}$$

We reference the diffusion coefficients for PTC to that of HOD in the sample to remove the effect of varying viscosity (*see* Supporting Information) and assume that the diffusion coefficient of the PTC molecules at a concentration of 5 mM corresponds to that of the monomer. We estimate the ratio of radii of the monomer and dimer using structures optimized with DFT calculations and HYDROPRO, finding $r_{dimer}/r_{monomer} = 1.05$. We assume that the oligomers grow proportionally larger by the same amount with each new molecule in the chain, which is a lower limit to its actual size. This estimate along with the calculated population fractions from the chemical shift fit provide a prediction free of fitting parameters for the effective radius in each model (Figure 5c). We can see that the modified dimer explains the data while the oligomer overestimates the size of the aggregates - so it is reasonable to assume that we have a system of dynamic dimers. We can then use the modified dimer model to fit the vibrational progression observed in the absorption (R_{abs}) with the model in equation 5 [23]:

$$R_{abs} = f_{\mathrm{monomer}} + f_{\mathrm{dimer}} \frac{(1-0.48^{g}/_{\omega_0})^2}{(1+0.146^{g}/_{\omega_0})^2} \qquad \text{(eq. 5)}$$

where g is the interchromophore coupling strength and ω_0 the frequency of the vibronic progression, in this case 1400 cm^{-1}. The fit for R_{abs} is shown on top of the experimental data in Figure 1b (red line) for a coupling constant of 259 cm^{-1}, in excellent agreement with the value of 250 cm^{-1} inferred from absorption broadening. The measured associated constant going from monomers to dimers is 8300 M^{-1}, which corresponds at 25ºC to a Gibbs energy of -22.36 kJ/mol.

Modelling molecular aggregation. The ^{1}H-NMR measurements cannot provide detailed information on the molecular organization, namely: distance, tilt, and twist angle between two molecules. We have run *ab initio* simulations to determine plausible structures to describe the behaviour observed. Given the solubility of PTC in water, the first tests were devoted to analysing the charge upon solution. We carried out a M06/6-31g simulation with water as implicit solvent and checked the agreement of the experimental and simulated absorption spectra, obtaining a charge of (-2) on opposite sides of the molecule to present the best agreement with experimental absorption (see supporting information). We scanned all potential geometries and found one main dimer conformation with an intramolecular hydrogen bond. Explicit water molecules had to be added due to the carboxylates to obtain representative results (see supporting information). The most stable structure was re-optimized and simulated in water with AIMD, in order to determine the variability in the twist and tilt angles (Figure 6). It resulted in a system exhibiting large conformational variation, with an average value of 37±10º for the twist angle, a range between 0º and 15º for the tilt angle, and an average distance of 4.5±0.2 Å (Figure 6c, d).

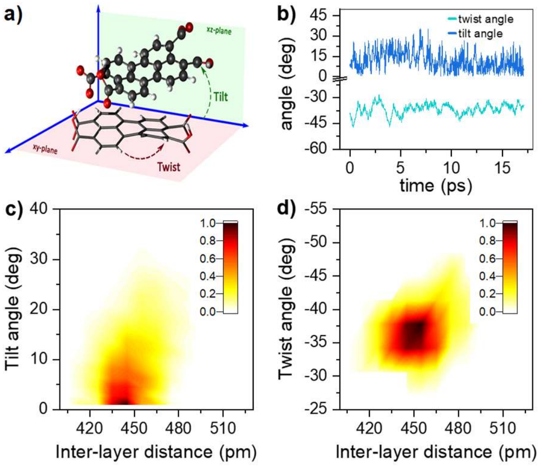

Figure 6. a) Schematic representation of the dimer twist and tilt angles considered (see S.I. for the formal definition). **b)** Temporal evolution of the twist and tilt angles (light and dark blue, respectively) along the AIMD trajectory at 300 K. Combined angular/radial probability of **c)** the twist angle and **d)** the tilt angle with respect to the distance between the two monomers computed from the 300K AIMD trajectory.

Modelling photophysical properties. Computed singlet and triplet transition energies for the PTC molecular dianion predict the feasibility of SF, as $E(S_1) \geq 2E(T_1)$ (*see* supporting information). In addition to the right energetics, SF requires the interaction between S_1 and the ^{1}(TT) state[14]. Interstate couplings evaluated for several conformations along the AIMD simulations for the lowest-energy dimer identify the viability of the formation of the triplet-pair state either by the direct $S_1 \rightarrow {}^1(TT)$ transition or through the mediation of CT states (Figure 7 c). The conformational flexibility produces a wide spread of couplings that are statistically summarized in figure 7(d) (*see* supporting information). Moreover, the structural flexibility of the PTC dimer, as described in the previous section, allows the system to easily explore a considerable section of the conformational space. These structural changes induce important fluctuations in state energies and interstate couplings. Although the accuracy of the performed RASCI calculations is limited, preventing us from predicting the exact state energies at each conformation unequivocally, it is worth noting that the energy fluctuations are large enough to induce changes in the energy ordering of the states, selectively promoting the stabilization of either S_1 or ^{1}(TT), or even inducing charge-separated configurations (CT states). In essence, the system's flexibility enables the exploration of a range of structures that may favor either of the deactivation pathways, namely SF or CT formation. Interestingly, excitonic couplings between the two local S_1 states in the dimer, although not directly involved in the SF process, are below 40 meV (322 cm^{-1}), in very good agreement with the broadening of absorption bands and the analysis of the vibrational progression.

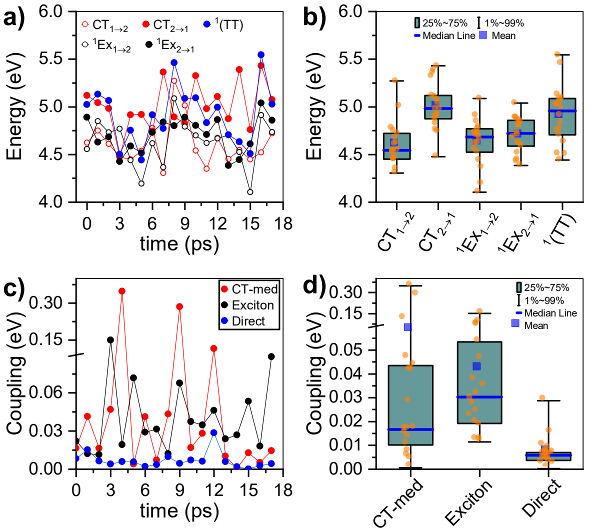

Figure 7. a,b) Fluctuations of diabatic state energies (in eV) and statistical dispersion parameters. **c,d)** Fluctuations of interstate couplings (in eV) computed along the AIMD dynamics of the lowest-energy PTC dimer and statistical dispersion parameters. V_{DC}: direct $S_1/^1(TT)$ SF-coupling (blue); V_{MC}: CT mediated SF-coupling (red); V_{ex}: exciton coupling (black).

Discussion

Our ^{1}H-NMR data are consistent with the formation of dimers mediated by the coordination of PTC with K^+ ions to form PTC-K_2. Theoretical modelling confirms the conformational flexibility, with a distribution of distances and twist & tilt angles. The excitation energy evolution of this disordered system can be reasonably well described by a target model, featuring the parallel evolution of only two deactivation pathways (DP1 & DP2 in Figure 8a). The deactivation rates of the singlets for each conformation are obtained from the streak camera (135±5ps & 20±5ps). To determine the formation rates of the new excited states for each deactivation pathway, we take advantage of the isosbestic point at 585 nm where only the new species absorb.

Figure 8b shows the kinetic trace at 585 nm, which can be fitted with three formation components (1, 28 & 148 ps). The 1 ps component suggests that a small proportion of the 600 nm ESA feature is formed from Hot-S_1. The target model was fitted globally, giving 39 % of deactivation path 1 (DP1) and 61 % of deactivation path 2 (DP2). For clarity, the *Species Associated Spectra* (SAS) are shown separately for each decay channel (Figure 8 c, d, respectively). After photoexcitation, a hot-S_1 is formed to evolve in 1 ps into ^{1}Ex(DP1) and ^{1}Ex(DP2). Surprisingly, the target analysis reveals notable differences between the two decay channels, not observable by sequential or parallel models. For DP1, ^{1}Ex(DP1) (green traces) generates a triplet state (blue traces, ESA ca. 605 nm) via singlet fission (k_{sf} = $(148\text{ ps})^{-1}$), which was already identified as a triplet excimer by sensitization measurements. The ^{1}Ex(DP1) SAS overlaps the Hot-S_1(DP1) SAS, apart from a small ESA in the 605 nm region. This would suggest that some of the triplet excimer is already formed from the Hot-S_1(DP1). For DP2, we observe remarkable differences for the 2nd and 3rd SAS (orange, red traces, respectively) as compared to DP1. The ^{1}Ex(DP2) SAS (orange traces) generates an excited state living 900 ps with no SE at 515 nm, and two ESA features at ca. 590 & 736 nm. The lack of fluorescence feature at 515 nm, and the long-living lifetime where no signal of fluorescence was recorded, suggest that the 736 nm ESA is not due to the $^1Ex_1$–^1Ex_n transition. These spectral features would be consistent with the formation of perylene cations and anions, i.e., a CT state[24, 62]. It is worth noting that ^{1}Ex(DP2) SAS shows a weak ESA at 590 nm, which might be related to the CT state formation from Hot-S_1(DP2).

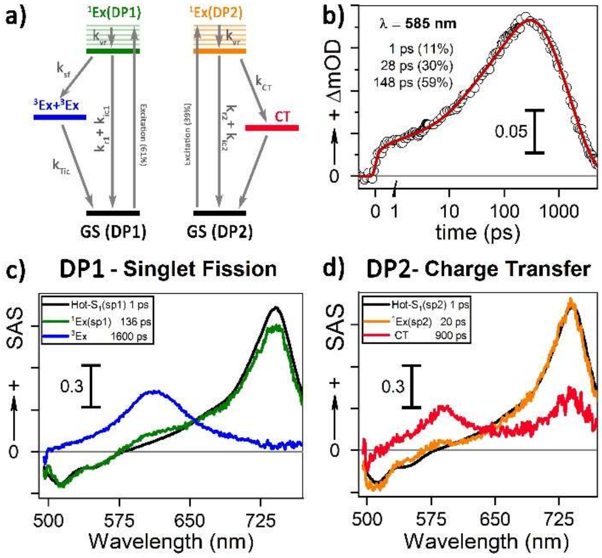

Figure 8. a) Target model for two parallel deactivation pathways. The electronic levels are color-coded with the associated SAS obtained from the global fitting. The system evolves as follows for DP1 (DP2): Hot-S_1 – grey (black), ^{1}Ex - green (orange), triplet excimer – blue, and charge transfer species - red. **b)** Kinetics and fitting of the isosbestic point (585 nm) for 90 mM PTC. **c, d)** SAS for 90 mM PTC with 415 nm excitation at 100 mW for DP1 & DP2, respectively.

From our computational analysis, the two possible decay channels of the photoexcited system, i.e., generation of two triplet excitons via SF (DP1) and formation of a CT state (DP2) can be rationalized by: (i) singlet-triplet energies adequate for SF, (ii) non-zero SF couplings, (iii) low energy CT states due to small intermolecular distances and strong polar medium, and (iv) dynamic fluctuations of state energies allowing for the simultaneous availability of DP1 and DP2. The presence of different geometries leading to two different processes (CT and SF) has been described for dimers of perylene[71] and PDI[72] in organic solvents. In molecular aggregates, overlapping wavefunctions on neighbouring molecules can lead to an additional CT-mediated exciton coupling with a vastly different spatial dependence and twist angle between two unslipped molecules. It has been shown that smaller changes in distance and twist & tilt angles than those modelled here can lead to a switch between CT and SF [62, 71]. However, further studies are necessary to assign each process to predominant conformations.

To calculate the efficiency of the processes (triplet and CT quantum yields; Φ_T, Φ_{CT}) in each conformation, we cannot rely on the change in ground state bleaching due to the overlapping with the excimer triplet ESA. The most reliable method to calculate the yields of triplets and charge separation is by using the formation rates described in equations 6, 7, and 8:

$$\frac{d[^1Ex]}{dt} = -\left(k_r + k_{ic} + k_{isc} + k_{sf} + k_{CT}\right)[^1Ex] \qquad \text{(eq. 6)}$$

$$\frac{d[^3Ex]}{dt} = (2 * k_{sf} + k_{isc})[^1Ex] \qquad \text{(eq. 7)}$$

$$\frac{d[CT]}{dt} = k_{CT}[^1Ex] \qquad \text{(eq. 8)}$$

The rate constants are denoted as follows: radiative deactivation (κ_r), internal conversion (κ_{ic}), inter-system crossing (κ_{isc}), singlet fission (κ_{sf}), and charge separation (κ_{CT}). The triplet and charge separation quantum yield are given by eqs. 9 & 10. We consider that κ_{isc} can be approximated to zero, since no triplet formation is detected in dilute solutions. The overall singlet deactivation process is described by the singlet decay rate, measured by fluorescence and called effective singlet decay (κ_{eff}).

$$\Phi_T = \frac{d[^3Ex]}{d[^1Ex]} = \frac{2*k_{sf}+k_{isc}}{k_r+k_{nr}+k_{isc}+k_{sf}+k_{CT}} = \frac{2*k_{sf}}{k_{eff}} \qquad \text{(eq. 9)}$$

$$\Phi_{CT} = \frac{d[CT]}{d[^1Ex]} = \frac{k_{CT}}{k_r+k_{nr}+k_{isc}+k_{sf}+k_{CT}} = \frac{k_{CT}}{k_{eff}} \qquad \text{(eq. 10)}$$

Table 1. Kinetic constants for the 90 mM sample obtained from the isosbestic point at 585 nm, effective singlet decay (κ_{eff}) obtained by the streak camera, and quantum yield for triplet formation and charge transfer.

	%	k_{CT} **(ps^{-1})**	k_{sf} **(ps^{-1})**	k_{eff} **(ps^{-1})**	**QY Triplet (%)**	**QY CT (%)**
DP1	61	N/A	$(148\pm10)^{-1}$	$(135\pm5)^{-1}$	182 ± 25	N/A
DP2	39	$(28\pm5)^{-1}$	N/A	$(20\pm5)^{-1}$	N/A	71 ± 15

Conclusions

Our research has provided pioneering evidence of singlet fission in aqueous solutions of perylene, and yields new insights into the photophysical properties of the system. Our results show that small changes in the molecular association modes can lead to different photophysical processes after photoexcitation such as singlet fission or charge transfer. We calculate that the efficiency of singlet fission / charge separation in aqueous perylene dimers depends strongly on their dynamic conformation, producing for DP1 an SF quantum efficiency close to 91 % (triplet formation 182%), and for DP2 a charge separation efficiency of 70 %. Overall, our study represents a major advance in the field of singlet fission and opens up exciting new directions for the development of water-compatible systems.

Conflicts of interest

There are no conflicts to declare.

Acknowledgements

This work was supported by the French Infrastructure for Integrated Structural Biology (FRISBI) ANR-10-INBS-05, the French National Research Agency (SINGLETFISSION grant N°: ANR-23-CE29-0007 and FISCIENCY grant N°: ANR-23-CE50-009), the CNRS 80PRIME interdisciplinary program, and ECOS-Nord program (action #M21P02). DFS acknowledges funding from PAPIIT IA202821. We acknowledge Elisabet Huerta for technical assistance. The authors thank the Grand Equipement National de Calcul Intensif (GENCI) French National Supercomputing Facility for computer time (project Grant A0140814154). R.A.B and D.C. acknowledge the Spanish Government MICINN (project PID2022-136231NB-I00), the Gipuzkoa Provincial Council (project QUAN-000021-01), the European Union (project NextGenerationEU/PRTR-C17.I1), as well as by the IKUR Strategy under the collaboration agreement between Ikerbasque Foundation and DIPC on behalf of the Department of Education of the Basque Government. D.C. is thankful for financial support from IKERBASQUE (Basque Foundation for Science). The authors are thankful for the technical and human support provided by the Donostia International Physics Center (DIPC) Computer Center.

ABBREVIATIONS

PTCDA, Perylene-3,4,9,10-tetracarboxylic dianhydride; PTC, perylene-3,4,9,10-tetracarboxylic acid; SF: Singlet-Fission; LE, Local excited state; CT, Charge-transfer state.

References

1. P. Anastas and N. Eghbali, Green Chemistry: Principles and Practice, *Chem. Soc. Rev.*, 2010, **39**, 301-312.
2. M. B. Smith and J. Michl, Singlet Fission, *Chem. Rev. (Washington, DC, U. S.)*, 2010, **110**, 6891-6936.
3. S. Singh, W. J. Jones, W. Siebrand, B. P. Stoicheff and W. G. Schneider, Laser Generation of Excitons and Fluorescence in Anthracene Crystals, *J. Chem. Phys.*, 1965, **42**, 330-342.
4. C. E. Swenberg and W. T. Stacy, Bimolecular radiationless transitions in crystalline tetracene, *Chem. Phys. Lett.*, 1968, **2**, 327-328.
5. N. Geacintov, M. Pope and F. Vogel, Effect of Magnetic Field on the Fluorescence of Tetracene Crystals: Exciton Fission, *Phys. Rev. Lett.*, 1969, **22**, 593-596.
6. R. E. Merrifield, P. Avakian and R. P. Groff, Fission of singlet excitons into pairs of triplet excitons in tetracene crystals, *Chem. Phys. Lett.*, 1969, **3**, 155-157.
7. M. C. Hanna and A. J. Nozik, Solar conversion efficiency of photovoltaic and photoelectrolysis cells with carrier multiplication absorbers, *J. Appl. Phys.*, 2006, **100**, 074510-074518.
8. A. J. Musser, M. Liebel, C. Schnedermann, T. Wende, T. B. Kehoe, A. Rao and P. Kukura, Evidence for conical intersection dynamics mediating ultrafast singlet exciton fission, *Nat. Phys.*, 2015, **11**, 352-357.
9. H. L. Stern, A. Cheminal, S. R. Yost, K. Broch, S. L. Bayliss, K. Chen, M. Tabachnyk, K. Thorley, N. Greenham, J. M. Hodgkiss, *et al.*, Vibronically coherent ultrafast triplet-pair formation and subsequent thermally activated dissociation control efficient endothermic singlet fission, *Nature Chem.*, 2017, **9**, 1205-1212.
10. C. B. Dover, J. K. Gallaher, L. Frazer, P. C. Tapping, A. J. Petty, M. J. Crossley, J. E. Anthony, T. W. Kee and T. W. Schmidt, Endothermic singlet fission is hindered by excimer formation, *Nature Chem.*, 2018, **10**, 305-310.
11. R. Pandya, Q. Gu, A. Cheminal, R. Y. S. Chen, E. P. Booker, R. Soucek, M. Schott, L. Legrand, F. Mathevet, N. C. Greenham, *et al.*, Optical Projection and Spatial Separation of Spin-Entangled Triplet Pairs from the S1 (21 Ag–) State of Pi-Conjugated Systems, *Chem*, 2020, **6**, 2826-2851.
12. A. J. Musser and J. Clark, Triplet-Pair States in Organic Semiconductors, *Annu. Rev. Phys. Chem.*, 2019, **70**, 323-351.
13. R. Casillas, I. Papadopoulos, T. Ullrich, D. Thiel, A. Kunzmann and D. M. Guldi, Molecular insights and concepts to engineer singlet fission energy conversion devices, *Energy & Environmental Science*, 2020, **13**, 2741-2804
14. D. Casanova, Theoretical Modeling of Singlet Fission, *Chem. Rev. (Washington, DC, U. S.)*, 2018, **118**, 7164-7207.
15. B. J. Walker, A. J. Musser, D. Beljonne and R. H. Friend, Singlet exciton fission in solution, *Nature Chem.*, 2013, **5**, 1019-1024.
16. H. L. Stern, A. J. Musser, S. Gelinas, P. Parkinson, L. M. Herz, M. J. Bruzek, J. Anthony, R. H. Friend and B. J. Walker, Identification of a triplet pair intermediate in singlet exciton fission in solution, *Proc. Natl. Acad. Sci.*, 2015, **112**, 7656-7661.
17. D. G. Bossanyi, M. Matthiesen, S. Wang, J. A. Smith, R. C. Kilbride, J. D. Shipp, D. Chekulaev, E. Holland, J. E. Anthony, J. Zaumseil, *et al.*, Emissive spin-0 triplet-pairs are a direct product of triplet–triplet annihilation in pentacene single crystals and anthradithiophene films, *Nature Chem.*, 2021, **13**, 163-171.
18. M. J. Y. Tayebjee, S. N. Sanders, E. Kumarasamy, L. M. Campos, M. Y. Sfeir and D. R. McCamey, Quintet multiexciton dynamics in singlet fission, *Nat. Phys.*, 2017, **13**, 182-188.
19. M. Dvořák, S. K. K. Prasad, C. B. Dover, C. R. Forest, A. Kaleem, R. W. MacQueen, A. J. Petty, R. Forecast, J. E. Beves, J. E. Anthony, *et al.*, Singlet Fission in Concentrated TIPS-Pentacene Solutions: The Role of Excimers and Aggregates, *J. Am. Chem. Soc.*, 2021, **143**, 13749-13758.

20. E. A. Margulies, J. L. Logsdon, C. E. Miller, L. Ma, E. Simonoff, R. M. Young, G. C. Schatz and M. R. Wasielewski, Direct Observation of a Charge-Transfer State Preceding High-Yield Singlet Fission in Terrylenediimide Thin Films, *J. Am. Chem. Soc.*, 2017, **139**, 663-671.
21. N. V. Korovina, S. Das, Z. Nett, X. Feng, J. Joy, R. Haiges, A. I. Krylov, S. E. Bradforth and M. E. Thompson, Singlet Fission in a Covalently Linked Cofacial Alkynyltetracene Dimer, *J. Am. Chem. Soc.*, 2016, **138**, 617-627.
22. A. M. Alvertis, S. Lukman, T. J. H. Hele, E. G. Fuemmeler, J. Feng, J. Wu, N. C. Greenham, A. W. Chin and A. J. Musser, Switching between Coherent and Incoherent Singlet Fission via Solvent-Induced Symmetry Breaking, *J. Am. Chem. Soc.*, 2019, **141**, 17558-17570.
23. N. J. Hestand and F. C. Spano, Expanded Theory of H- and J-Molecular Aggregates: The Effects of Vibronic Coupling and Intermolecular Charge Transfer, *Chem. Rev. (Washington, DC, U. S.)*, 2018, **118**, 7069-7163.
24. I. Papadopoulos, D. Gutiérrez-Moreno, Y. Bo, R. Casillas, P. M. Greißel, T. Clark, F. Fernández-Lázaro and D. M. Guldi, Altering singlet fission pathways in perylene-dimers; perylene-diimide versus perylene-monoimide, *Nanoscale*, 2022, **14**, 5194-5203.
25. M. Grzybowski and D. T. Gryko, Diketopyrrolopyrroles: Synthesis, Reactivity, and Optical Properties, *Advanced Optical Materials*, 2015, **3**, 280-320.
26. M. J. Y. Tayebjee, K. N. Schwarz, R. W. MacQueen, M. Dvořák, A. W. C. Lam, K. P. Ghiggino, D. R. McCamey, T. W. Schmidt and G. J. Conibeer, Morphological Evolution and Singlet Fission in Aqueous Suspensions of TIPS-Pentacene Nanoparticles, *J. Phys. Chem. C*, 2016, **120**, 157-165.
27. R. J. Hudson, J. M. de la Perrelle, R. D. Pensack, B. Kudisch, G. D. Scholes, D. M. Huang and T. W. Kee, Organizing Crystalline Functionalized Pentacene Using Periodicity of Poly(Vinyl Alcohol), *J. Phys. Chem. Lett.*, 2020, **11**, 516-523.
28. R. J. Hudson, A. N. Stuart, J. M. de la Perrelle, D. M. Huang and T. W. Kee, Nanoparticle Size-Dependent Singlet Fission and Exciton Dynamics in Amorphous TIPS-Pentacene, *J. Phys. Chem. C*, 2021, **125**, 21559-21570.
29. A. J. Musser, M. Maiuri, D. Brida, G. Cerullo, R. H. Friend and J. Clark, The Nature of Singlet Exciton Fission in Carotenoid Aggregates, *J. Am. Chem. Soc.*, 2015, **137**, 5130-5139.
30. A. Quaranta, A. Krieger-Liszkay, A. A. Pascal, F. Perreau, B. Robert, M. Vengris and M. J. Llansola-Portoles, Singlet fission in naturally-organized carotenoid molecules, *Phys. Chem. Chem. Phys.*, 2021, **23**, 4768-4776.
31. M. J. Llansola-Portoles, K. Redeckas, S. Streckaite, C. Ilioaia, A. A. Pascal, A. Telfer, M. Vengris, L. Valkunas and B. Robert, Lycopene crystalloids exhibit singlet exciton fission in tomatoes, *Phys. Chem. Chem. Phys.*, 2018, **20**, 8640 - 8646.
32. A. Ortega, D. Amorós and J. García de la Torre, Prediction of hydrodynamic and other solution properties of rigid proteins from atomic- and residue-level models, *Biophys. J.*, 2011, **101**, 892-898.
33. M. J. Frisch, G. W. Trucks, H. B. Schlegel, G. E. Scuseria, M. A. Robb, J. R. Cheeseman, G. Scalmani, V. Barone, G. A. Petersson, H. Nakatsuji*, et al.*, Gaussian 16 Rev. C.01.*Journal*, 2019.
34. J. Tomasi and M. Persico, Molecular Interactions in Solution: An Overview of Methods Based on Continuous Distributions of the Solvent, *Chem. Rev. (Washington, DC, U. S.)*, 1994, **94**, 2027-2094.
35. J. F. Pérez, C. Z. Hadad and A. Restrepo, Structural studies of the water tetramer, *Int. J. Quantum Chem.*, 2008, **108**, 1653-1659.
36. J. Pérez and A. Restrepo, ASCEC V–02: Annealing Simulado con Energía Cuántica, *Property, development and implementation: Grupo de Química–Física Teórica, Instituto de Química, Universidad de Antioquia: Medellín, Colombia*, 2008.
37. Y. Zhao and D. G. Truhlar, A new local density functional for main-group thermochemistry, transition metal bonding, thermochemical kinetics, and noncovalent interactions, *J. Chem. Phys.*, 2006, **125**.
38. J. S. Binkley, J. A. Pople and W. J. Hehre, Self-consistent molecular orbital methods. 21. Small split-valence basis sets for first-row elements, *J. Am. Chem. Soc.*, 1980, **102**, 939-947.
39. J. M. Martínez and L. Martínez, Packing optimization for automated generation of complex system's initial configurations for molecular dynamics and docking, *J. Comput. Chem.*, 2003, **24**, 819-825.
40. L. Martínez, R. Andrade, E. G. Birgin and J. M. Martínez, PACKMOL: A package for building initial configurations for molecular dynamics simulations, *J. Comput. Chem.*, 2009, **30**, 2157-2164.
41. J. P. Perdew, K. Burke and M. Ernzerhof, Generalized Gradient Approximation Made Simple, *Phys. Rev. Lett.*, 1996, **77**, 3865-3868.
42. S. Grimme, J. Antony, S. Ehrlich and H. Krieg, A consistent and accurate ab initio parametrization of density functional dispersion correction (DFT-D) for the 94 elements H-Pu, *J. Chem. Phys.*, 2010, **132**.
43. S. Grimme, S. Ehrlich and L. Goerigk, Effect of the damping function in dispersion corrected density functional theory, *J. Comput. Chem.*, 2011, **32**, 1456-1465.
44. S. Goedecker, M. Teter and J. Hutter, Separable dual-space Gaussian pseudopotentials, *Physical Review B*, 1996, **54**, 1703-1710.
45. J. VandeVondele, M. Krack, F. Mohamed, M. Parrinello, T. Chassaing and J. Hutter, Quickstep: Fast and accurate density functional calculations using a mixed Gaussian and plane waves approach, *Comput. Phys. Commun.*, 2005, **167**, 103-128.
46. C. Hartwigsen, S. Goedecker and J. Hutter, Relativistic separable dual-space Gaussian pseudopotentials from H to Rn, *Physical Review B*, 1998, **58**, 3641-3662.
47. S. Nosé, A molecular dynamics method for simulations in the canonical ensemble, *Mol. Phys.*, 1984, **52**, 255-268.
48. W. Humphrey, A. Dalke and K. Schulten, VMD: Visual molecular dynamics, *Journal of Molecular Graphics*, 1996, **14**, 33-38.
49. M. Brehm, M. Thomas, S. Gehrke and B. Kirchner, TRAVIS—A free analyzer for trajectories from molecular simulation, *J. Chem. Phys.*, 2020, **152**.
50. M. Brehm and B. Kirchner, TRAVIS - A Free Analyzer and Visualizer for Monte Carlo and Molecular Dynamics Trajectories, *J. Chem. Inf. Model.*, 2011, **51**, 2007-2023.
51. E. Epifanovsky, A. T. B. Gilbert, X. Feng, J. Lee, Y. Mao, N. Mardirossian, P. Pokhilko, A. F. White, M. P. Coons, A. L. Dempwolff*, et al.*, Software for the frontiers of quantum chemistry: An overview of developments in the Q-Chem 5 package, *J. Chem. Phys.*, 2021, **155**.
52. A. Carreras, O. Uranga-Barandiaran, F. Castet and D. Casanova, Photophysics of Molecular Aggregates from Excited State Diabatization, *J. Chem. Theory Comput.*, 2019, **15**, 2320-2330.
53. D. Casanova and M. Head-Gordon, Restricted active space spin-flip configuration interaction approach: theory, implementation and examples, *Phys. Chem. Chem. Phys.*, 2009, **11**, 9779-9790.
54. D. Casanova, Restricted active space configuration interaction methods for strong correlation: Recent developments, *WIREs Computational Molecular Science*, 2022, **12**, e1561.

55. R. Krishnan, J. S. Binkley, R. Seeger and J. A. Pople, Self-consistent molecular orbital methods. XX. A basis set for correlated wave functions, *J. Chem. Phys.*, 1980, **72**, 650-654.
56. S. F. Boys, Construction of Some Molecular Orbitals to Be Approximately Invariant for Changes from One Molecule to Another, *Rev. Mod. Phys.*, 1960, **32**, 296-299.
57. V. Dehm, Z. Chen, U. Baumeister, P. Prins, L. D. A. Siebbeles and F. Würthner, Helical Growth of Semiconducting Columnar Dye Assemblies Based on Chiral Perylene Bisimides, *Org. Lett.*, 2007, **9**, 1085-1088.
58. P. P. N. Syamala, B. Soberats, D. Görl, S. Gekle and F. Würthner, Thermodynamic insights into the entropically driven self-assembly of amphiphilic dyes in water, *Chemical Science*, 2019, **10**, 9358-9366.
59. F. C. Spano, The Spectral Signatures of Frenkel Polarons in H- and J-Aggregates, *Acc. Chem. Res.*, 2010, **43**, 429-439.
60. C. R. Cantor and P. Schimmel, in *Biophysical Chemistry: Part II: Techniques for the Study of Biological Structure and Function*, 1980.
61. N. V. Korovina, C. H. Chang and J. C. Johnson, Spatial separation of triplet excitons drives endothermic singlet fission, *Nature Chem.*, 2020, **12**, 391-398.
62. E. A. Margulies, C. E. Miller, Y. Wu, L. Ma, G. C. Schatz, R. M. Young and M. R. Wasielewski, Enabling singlet fission by controlling intramolecular charge transfer in π-stacked covalent terrylenediimide dimers, *Nature Chem.*, 2016, **8**, 1120-1125.
63. R. E. Cook, B. T. Phelan, R. J. Kamire, M. B. Majewski, R. M. Young and M. R. Wasielewski, Excimer Formation and Symmetry-Breaking Charge Transfer in Cofacial Perylene Dimers, *J. Phys. Chem. A*, 2017, **121**, 1607-1615.
64. W. Ni, G. G. Gurzadyan, J. Zhao, Y. Che, X. Li and L. Sun, Singlet Fission from Upper Excited Electronic States of Cofacial Perylene Dimer, *J. Phys. Chem. Lett.*, 2019, **10**, 2428-2433.
65. Z. Yu, Y. Wu, Q. Peng, C. Sun, J. Chen, J. Yao and H. Fu, Accessing the Triplet State in Heavy-Atom-Free Perylene Diimides, *Chemistry – A European Journal*, 2016, **22**, 4717-4722.
66. K. Nagarajan, A. R. Mallia, V. S. Reddy and M. Hariharan, Access to Triplet Excited State in Core-Twisted Perylenediimide, *J. Phys. Chem. C*, 2016, **120**, 8443-8450.
67. C. Flors and S. Nonell, On the Phosphorescence of 1H-Phenalen-1-one, *Helv. Chim. Acta*, 2001, **84**, 2533-2539.
68. A. D. Bain, Chemical exchange in NMR, *Prog. Nucl. Magn. Reson. Spectrosc.*, 2003, **43**, 63-103.
69. A. D. Shaller, W. Wang, H. Gan and A. D. Q. Li, Tunable Molecular Assembly Codes Direct Reaction Pathways, *Angew. Chem. Int. Ed.*, 2008, **47**, 7705-7709.
70. W. Wang, J. J. Han, L.-Q. Wang, L.-S. Li, W. J. Shaw and A. D. Q. Li, Dynamic π−π Stacked Molecular Assemblies Emit from Green to Red Colors, *Nano Lett.*, 2003, **3**, 455-458.
71. N. J. Hestand and F. C. Spano, Interference between Coulombic and CT-mediated couplings in molecular aggregates: H- to J-aggregate transformation in perylene-based π-stacks, *J. Chem. Phys.*, 2015, **143**, 244707.
72. J. Idé, R. Méreau, L. Ducasse, F. Castet, Y. Olivier, N. Martinelli, J. Cornil and D. Beljonne, Supramolecular Organization and Charge Transport Properties of Self-Assembled π−π Stacks of Perylene Diimide Dyes, *J. Phys. Chem. B*, 2011, **115**, 5593-5603.

Supporting Information

Perylene singlet exciton fission in water solution

Chloe Magne[a], Simona Streckaite[b], Roberto A. Boto[c], Eduardo Domínguez-Ojeda[d], Marina Gromova[e], Andrea Echeverri[f], Flavio Siro Brigiano[f], Minh-Huong Ha-Thi[g], Marius Fanckevičius[b], Vidmantas Jašinskas[b], Annamaria Quaranta[a], Andrew A. Pascal[a], Matthieu Koepf[h], David Casanova[c,i], Thomas Pino[g], Bruno Robert[a], Julia Contreras-García[f], Daniel Finkelstein-Shapiro[d], Vidmantas Gulbinas[b], Manuel J. Llansola-Portoles[a]*

[a]*Université Paris-Saclay, CEA, CNRS, Institute for Integrative Biology of the Cell (I2BC), 91198Gif-sur-Yvette, France.*

[b]*Department of Molecular Compound Physics, Center for Physical Sciences and Technology, Saulėtekio Avenue 3, LT-10257 Vilnius, Lithuania*

[c]*Donostia International Physics Center (DIPC), 20018 Donostia, Euskadi, Spain.*

[d]*Insituto de Química, Universidad Nacional Autónoma de México, 04510 Mexico City, Mexico*

[e]*Université Grenoble Alpes, CNRS, CEA, IRIG, MEM, F-38054 Grenoble, France*

[f]*Sorbonne Université, CNRS, Laboratoire de Chimie Théorique, LCT, F. 75005 Paris, France*

[g]*Université Paris-Saclay, CNRS, Institut des Sciences Moléculaires d'Orsay, 91405 Orsay, France.*

[h]*Université Grenoble Alpes, CNRS, CEA, IRIG, Laboratoire de Chimie et Biologie des Métaux, F-38054 Grenoble, France*

[i]*IKERBASQUE, Basque Foundation for Science, 48009 Bilbao, Euskadi, Spain.*

*Corresponding author. manuel.llansola@i2bc.paris-saclay.fr

Table of Contents

1. Synthesis of perylene-3,4,9,10-tetracarboxylate 3
2. Steady-State Absorption and Fluorescence 3
3. Determination of specific molar absorptivity 5
4. Time-Resolved Fluorescence (SPC) 6
5. Time-Resolved Fluorescence (streak camera) 7
6. Femto- to nano-second Transient Absorption Spectroscopy 8
    6.1. Global Analysis – Sequential fit 8
    6.2. Global Analysis – Parallel fit 10
    6.3. Power intensity 12
7. Determination of triplet by sensitization 12
8. Nuclear Magnetic Resonance 14
    8.1. ^{1}H-NMR measurements at different concentrations 14
    8.2. Modelling of PTC association 17
    8.3. DOSY experiments 20
9. Molecular Simulations 23
    9.1. Monomer Conformations 23
    9.2. Dimer Conformation 25
    9.3. Assessing the performance of M06 functional 28
    9.4. Discussion on S_1 and T_1 energies for the PTC monomer 28
    9.5. Evolution of excitation energies and electronic couplings with the time 29
10. References 32

1. Synthesis of perylene-3,4,9,10-tetracarboxylate

We synthetized a water-soluble perylene by hydrolyzing 3,4,9,10-perylenetetracarboxylic dianhydride to yield a perylene-3,4,9,10-tetracarboxylic(Hernández, Godin et al. 2013). The reagents and materials for the synthesis were purchased from Sigma Aldrich. Perylene-3,4,9,10-tetracarboxylic dianhydride (PTCDA), and KOH were used as received, with a purity of 97% and 90% respectively. To prepare the most concentrated solution of perylene-3,4,9,10-tetracarboxylate (90 mM), we added 350mg PTCDA to 10mL of 0.5M KOH solution in Milli-Q water, and sonicated for 45min at room temperature to induce the following reaction:

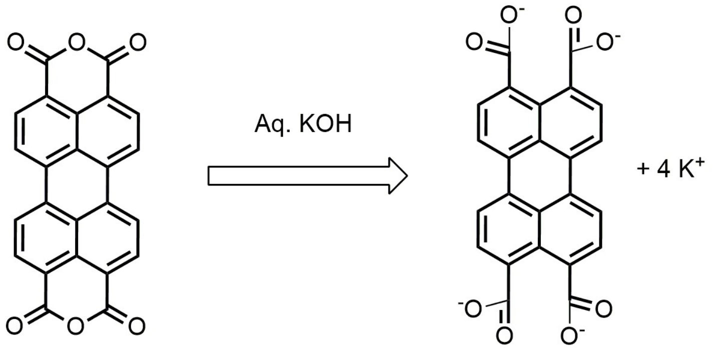

To minimize experimental error in the sample preparation, the most concentrated solution (90 mM) was used to prepare the set of diluted samples in 0.1 M KOH. Each solution was also sonicated for 10 min between dilutions and prior to each measurement.

2. Steady-State Absorption and Fluorescence

The concentrations studied for steady state absorption and fluorescence are: 0.01mM, 0.1mM, 1mM, 10mM, 30mM, 45mM, 60mM and 90mM. It must be noted that preparing solutions higher than 90 mM surpasses the solubility limit and produces a red paste. The study of the concentrated paste is out of the scope of this work. Note that to keep the absorption maxima below 1.5, and avoid saturation, we employed cuvettes/cells with different optical path lengths from 0.01 to 10 mm.

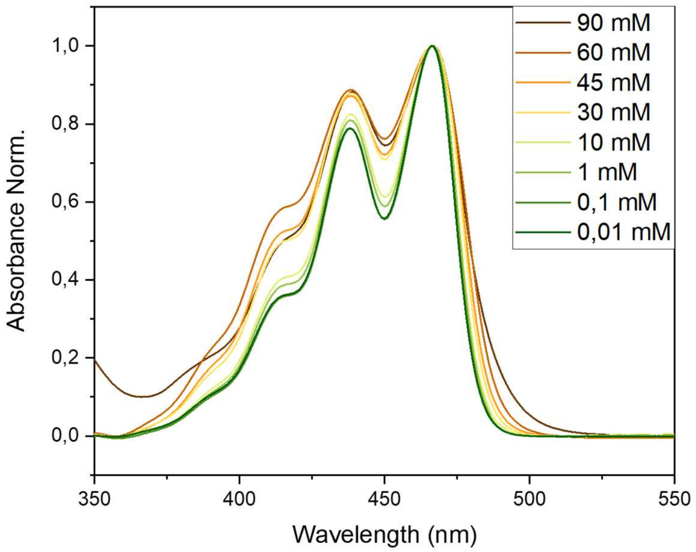

Figure S1 | Absorption spectra (specific molar absorptivity) at room temperature of perylene tetracarboxylate at 10, 30, 45, 60, and 90 mM in water solution at pH 13.

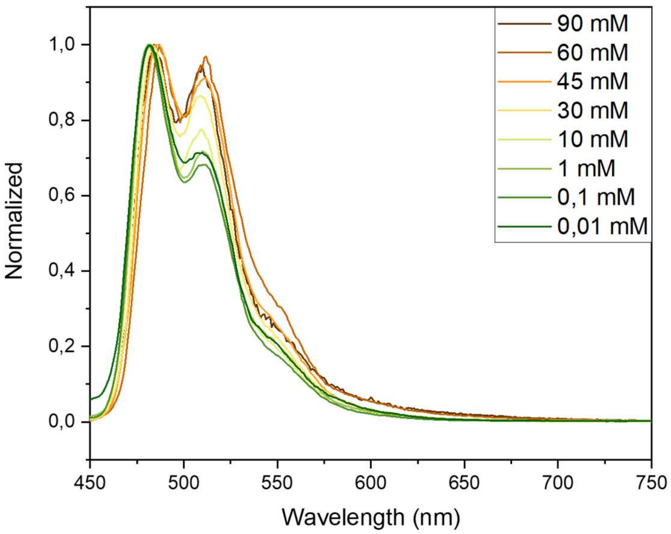

Figure S2 | Normalized fluorescence spectra at room temperature of perylene tetracarboxylate at 10, 30, 45, 60, and 90 mM in water solution at pH 13.

3. Determination of specific molar absorptivity

Calculation of the molar extinction coefficient for the different concentrations studied (0.01, 0.1, 1, 10, 30, 45, 60 and 90 mM). Use of the Beer-Lambert formula linking Absorbance, molar extinction coefficient ($M^{-1}.cm^{-1}$), optical path length and concentration:

$$A = \varepsilon . l . C \qquad \text{(eq. S1)}$$

For these measurements, different cells with different optical path lengths were used (from 0.01 to 10 mm). Details of the measurements carried out and the conditions used are shown in table S1. The results of the ratio of the line strengths of the first two vibronic peaks in the absorption R_{abs}, are also shown in Table S1.

$$R_{Abs} = \frac{I_{A_1}}{I_{A_2}} \qquad \text{(eq. S2)}$$

Table S1. Calculated molar extinction coefficient and R_{abs} for the different concentrations studied.

Concentrations (mM)	90	60	45	30	10	1	0.1	0.01
Cuvette Pathway (mm)	0.01	0.01	0.01	0.01	0.01	0.1	1	10
Absorbance (466nm)	0.908	1.051	1.165	0.840	0.318	0.305	0.426	0.435
Epsilon (466nm) ($M^{-1}.cm^{-1}$)	9771	17122	25062	27383	34254	32896	45905	46831

4. Time-Resolved Fluorescence (SPC)

Pico-to-nanosecond time-resolved fluorescence measurements were performed with an Edinburgh F920 (Edinburgh Instruments, UK) spectrometer. Fluorescence decay kinetics were obtained using time-correlated single photon counting (TCSPC). The excitation source was a picosecond-pulsed diode laser EPL-375 (Edinburgh Instruments, UK) emitting ~60 ps pulses (5 MHz repetition rate). The temporal resolution of this system was a few hundred ps.

To minimize self-absorption effects due to the high concentration, the samples were placed between two slices of glass ($OD_{465nm} < 0.15$). The decay of the fluorescence was recorded between 440-650 nm, and the intensity (I) with time (t) was fitted globally using equation S3:

$$I_{Fluorescence}\,(\lambda, t) = A_1(\lambda) * e^{-\frac{t}{\tau_1}} + A_2(\lambda) * e^{-\frac{t}{\tau_2}} \qquad \text{(eq. S3)}$$

where τ_1 and τ_2 are the lifetimes of different species, and A_1 and A_2 are their respective amplitudes for each wavelength.

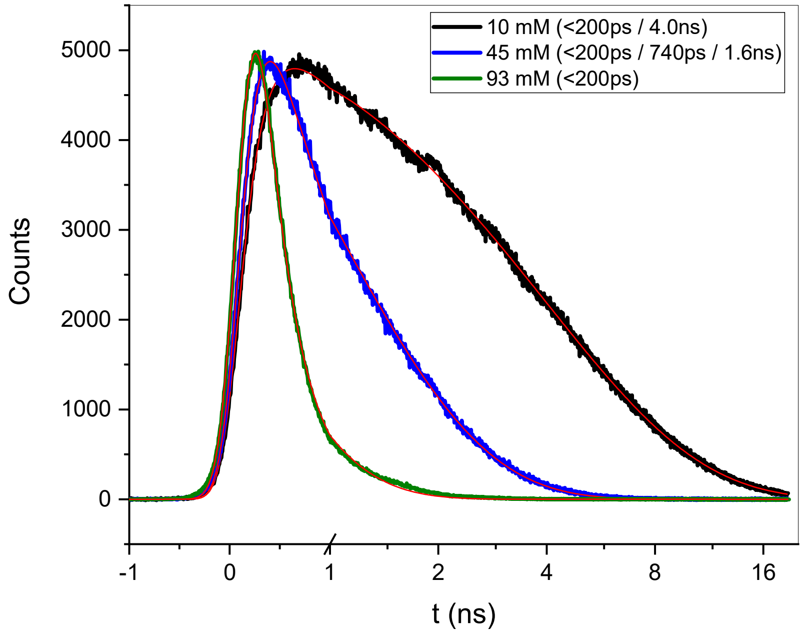

Figure S*3* | Time resolved fluorescence (Single Photon Counting) collected at 515 nm at 415 nm excitation.

5. Time-Resolved Fluorescence (streak camera)

Picosecond time-resolved fluorescence measurements were performed by using a streak camera system (Hamamatsu C5680) with synchroscan (M5675) unit coupled to a spectrometer. A femtosecond Yb:KGW oscillator (Light Conversion Ltd., Lithuania) generating 80 fs duration pulses at 1030 nm, which were frequency tripled to 343 nm (HIRO harmonics generator, Light Conversion Ltd.) at repetition rate of 76 MHz, was used for the sample excitation. Excitation energy density was attenuated using neutral density filters to about 15 nJ·cm^{-2}. The time resolution of the system was ≈8 ps. Signal acquisition time was 1-3 h for each measurement.

The decay times longer than 200 ps were obtained precisely by SPC, and then used as fixed parameters to obtain accurate values of the fastest rates. However, the 90 mM system is highly quenched and has no component longer than 200 ps. The data set needs invariably two components to yield a good fit. However, the shortest component produces good fits in the range from 15-to-25 ps as shown in figure S4. We use this range to obtain the error in the subsequent calculation of quantum yields.

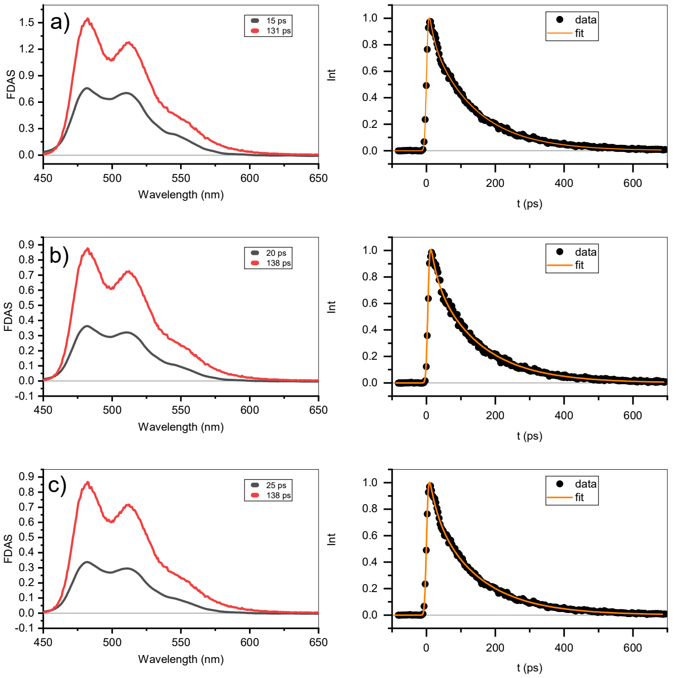

Figure S4 | Fluorescence time resolved (Streak Camera) FDAS and kinetics at 480 nm for 90 mM sample excited at 343 nm. Each panel shows several fittings to calculate the error decay error.

6. Femto- to nano-second Transient Absorption Spectroscopy

6.1. Global Analysis – Sequential fit

The evolution of excited states after photoexcitation at 415 nm was fitted globally to a sequential model. Figure S5 shows the *evolution decay associated spectra* (EDAS), and selected kinetics for 10 mM, 45 mM, and 90 mM. The 10 mM can be described by a three-component model (1 ps → 200 ps → 4.0 ns) with identical EDAS. A positive feature at 740 nm due to *excited-state-absorption* (ESA) is attributed to the S_1–S_n transition, and the negative features at 515 nm correspond to *stimulated emission* (SE). The first EDAS (1 ps) shows a slight bigger ESA, this be interpreted as a relaxation of vibrationally hot-S_1. The second EDAS (200 ps) can be reasonably assigned to an excimer with strong fluorescence quenching, and the third EDAS (4.0 ns) to the monomer. It must be noted that for weak excitonic interactions, as in the present case, it has been reported that the S_1–S_n and $^1Ex_1$–^1Ex_n transitions produce indistinguishable electronic signatures (Walker, Musser et al. 2013, Margulies, Miller et al. 2016, Korovina, Chang et al. 2020). This effect is particularly evident in the work of Marguilles *et al* (Margulies, Miller et al. 2016), where the absorption spectrum of the weakly-interacting dyad shows minimal changes compared to the monomer, whereas strongly-interacting dyads exhibit distorted absorption profiles and a distinctive $^1Ex_1$–^1Ex_n transition. The spectral signatures of the S_1–S_n and $^1Ex_1$–^1Ex_n transitions create an isosbestic point at 585 nm (ΔOD = 0).

The 45 mM sample shows a dataset with a positive feature at 740 nm that disappears in conjunction with an ESA increase at 605 nm. A 5-component sequential model yields a time evolution of 1 ps → 60 ps → 740 ps → 1.8 ns. The overall evolution shows that the two initial EDAS (1 ps, 60 ps) assigned to hot-S_1, and S_1, decay to the ground state since no further evolution of species is observed. However, for the 3rd and 4th EDAS (740 ps → 1.8 ns), there is a growing ESA that peaks at 605 nm which can be interpreted as the S_1 forming an unknown specie absorbing at 605 nm. The 4th EDAS corresponds mainly to decay of this unknown species, which is not fluorescent (not detected by streak camera or SPC). Hence, the presence of significant ESA at 740 nm indicates that the sequential model cannot reproduce the observations satisfactorily.

The 90 mM sample can be fitted to a 4-component sequential model with a time evolution of 1 ps → 25 ps → 135 ps → 1.6 ns. The 1st and 2nd EDAS (1 ps, and 25 ps) show a decay of the 740 nm feature (S_1-S_n), a negative feature at 515 nm due to SE, and a small increase in the 580-610 nm region.

The 3rd EDAS (135 ps) has a strong ESA feature growing in the 580-610 nm region simultaneously with decay of the 740 nm ESA and 515 nm SE features. The 4th EDAS (1.6 ns) corresponds to the decay of the unidentified 605 nm non-fluorescent species. The fitting of the datasets to sequential models is helpful to understand the evolution of the system at different concentrations, but it cannot describe the physical processes occurring. It is clear that the S_1 state deactivates by several parallel processes.

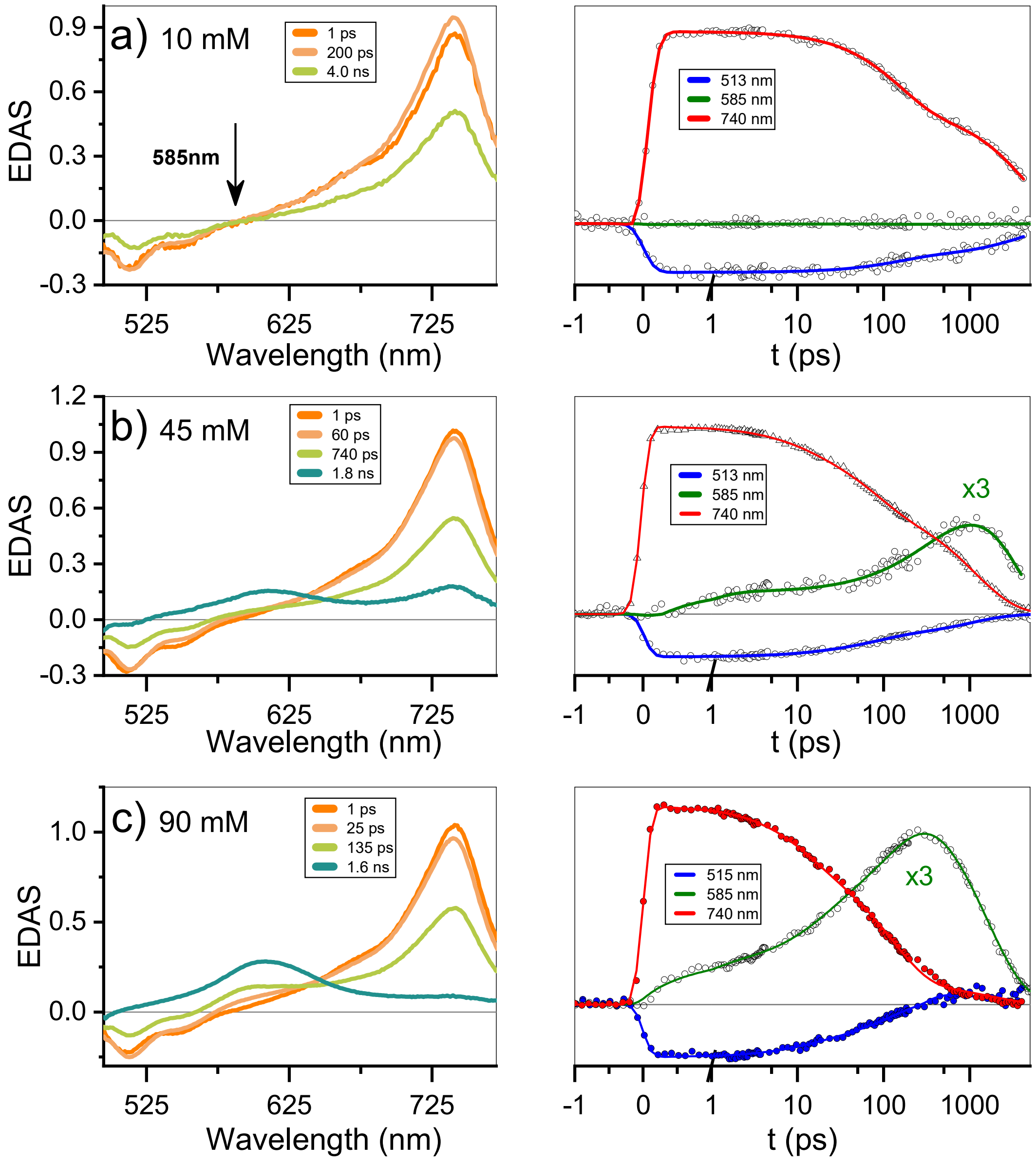

Figure S*5* | Transient absorption spectra of perylene in the fs-to-ns window: EDAS, and kinetics at 515, 585, and 740 nm for **a)** 10 mM, **b)** 45 mM, **c)** 90 mM solution. Excitation wavelength:415 nm; power: 100 mW.

6.2. Global Analysis – Parallel fit

The evolution of excited states after photoexcitation at 415 nm was fitted globally to a parallel model. Figure S6 shows the *evolution decay associated spectra* (DAS), and selected kinetics for the 10 mM, 45 mM, and 90 mM samples. The data at 10 mM can be described by a three-component model (1 ps, 200 ps, 4.0 ns). It is striking that the fast component for 740nm S_1–S_n transition is negative. It hints that there is an energy transfer between two species having the same S_1–S_n transition, in which one of them could have a slightly higher absorption. This could be interpreted as energy transfer between slightly different PTC dimers. However, this is out of the scope of this paper and the interpretation will be left for further studies of the system. Then, there are two decay components for the (positive) 740nm ESA and (negative) 515nm SE features, at 200 ps and 4.0 ns. The system at this concentration returns to the ground state without forming any intermediate species. It reinforces the interpretation from the sequential model, that the system contains monomers and dimers, decaying in 4 ns and 200 ps, respectively. The 45 mM sample shows a convoluted dataset with a positive feature at 740 nm that disappears along with a small ESA growth at 605 nm. The spectral signatures do not have any clear interpretation, suggesting that the parallel model is not able to capture the physical phenomena occurring with any certainty.

The 90 mM sample can be fitted to a 4-component parallel model to yield four components, decaying at 1 ps, 25 ps, 135 ps, and 1.6 ns. The 1st and 2nd DAS (1 and 25 ps) show a decay of the 740 nm feature (S_1-S_n), a negative feature at 515 nm due to SE, and a small negative feature in the 580-610 nm region peaking at 595 nm. This DAS reveals that the 580-620 nm feature is associated with the decay of the S_1–S_n transition. The 3rd DAS (135 ps) has a strong negative feature in the 580-620 nm region peaking at 610 nm, associated with decay of the 740 nm ESA and 515 nm SE. It is worth noting that the maximum of the negative feature for the 2nd and 3rd DAS are 15 nm shifted, which could indicate the formation of two different species. The 4th EDAS (1.6 ns) is the decay of the unidentified 605 nm non-fluorescent species (see above). The parallel model yields valuable insight into the different species formed, but it is still not able to capture the physical process(es) occurring. Hence, we need to develop more sophisticated schemes (see main text) to explain the observations.

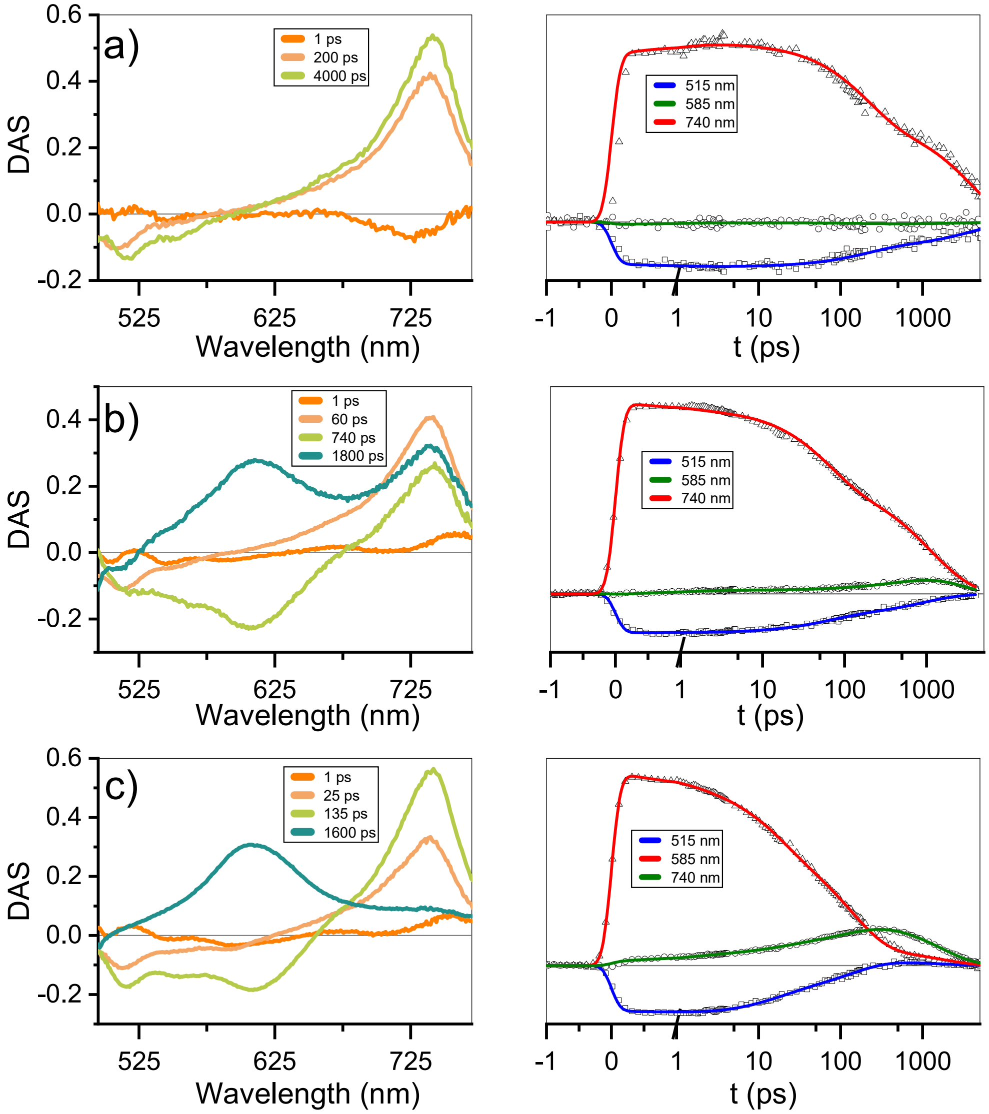

Figure S6 | Transient absorption spectra of perylene in the fs-to-ns window: DAS, and kinetics at 515, 585, and 740 nm for **a)** 10 mM, **b)** 45 mM, and **c)** 90 mM solution. Excitation wavelength at 415 nm and power 100 mW.

6.3. Power intensity

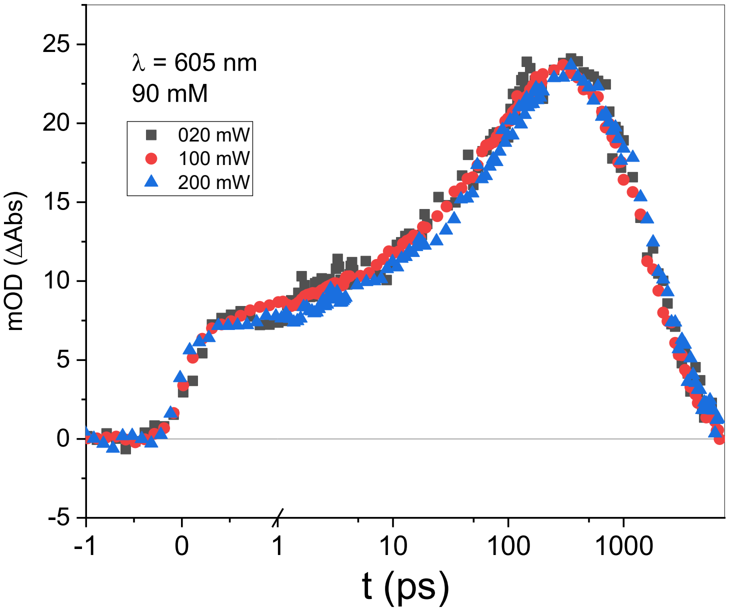

Figure S7 | Kinetic trace for 90 mM sample at 605 nm (excitation: 415 nm; power: 20, 100, and 200 mW).

7. Determination of triplet by sensitization

Sensitization measurements to unequivocally assign the signal at 600nm to a triplet were performed using 1H-Phenalen-1-One (CAS 548-39-0) supplied by Sigma-Aldrich with 97% purity. PTC is already at its solubility limit at 90 mM, so in order to carry out the measurements in solution we had to modify the conditions of the sample as follows.

In a 70:30 water-ethanol mixture, we introduced 45mM PTC and 45mM 1H-Phenalen-1-One. The sensitization measurements were performed by exciting into the phenalenone absorption band at 350 nm. Excited phenalenone molecules de-excite to the triplet state by intersystem crossing, with a yield close to 100%. Phenalenone triplets have a higher energy than PTC triplets, and so Triplet-Triplet energy transfer populates PTC triplet states (Knibbe, Rehm et al. 1968, Watkins 1974, Murov, Carmichael et al. 1993, Oliveros, H. Bossmann et al. 1999, Flors and Nonell 2001).

Table S2. Photophysical and energetic parameters of perylene (CAS 198-55-0) and 1H-Phenalen-1-one in different solvents (Knibbe, Rehm et al. 1968, Watkins 1974, Murov, Carmichael et al. 1993, Oliveros, H. Bossmann et al. 1999, Flors and Nonell 2001).

	Solvent	E_S (kJ/mol)	Qy fl	t_S (ns)	Qy T	E_T (kJ/mol)
Perylene	n	275	0.75	6.4	0.014	148
Perylene	p	273	0.87	6.0	0.0088	151
1H-Phenalen-1-one	Methyl-cyclohexane	299	≅ 0	-	≅ 1	185
1H-Phenalen-1-one	ethanol	299	≅ 0	-	≅ 1	186

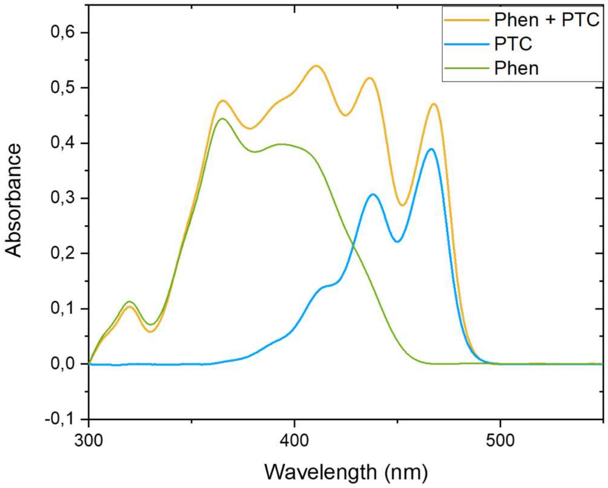

Figure S8 | Absorption Spectra of PTC, Phenaleone and the Phenalenone-PTC mixture in 70:30 water-ethanol solution (blue, green and yellow, respectively).

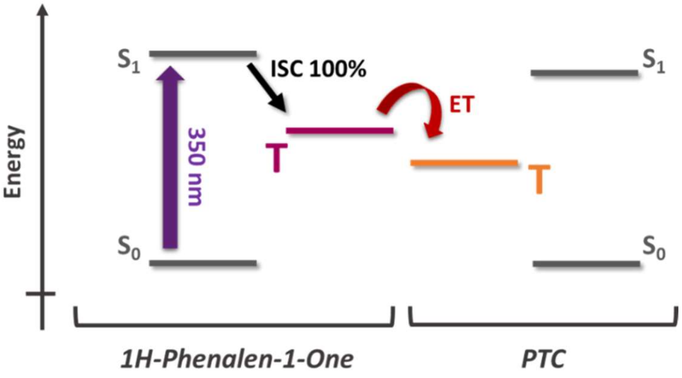

Figure S9 | Energetic Scheme for T-T sensitization from 1H-Phenalen-1-one to PTC after 350 nm excitation.

8. Nuclear Magnetic Resonance

8.1. ^{1}H-NMR measurements at different concentrations.

The ^{1}H-NMR spectra for all studied concentrations show a single chemical shift per distinguishable proton, an evidence of fast exchange between the different species. The individual spectra for each concentration are shown in Figs. S11-S14, and the chemical shifts are reported in Table S3.

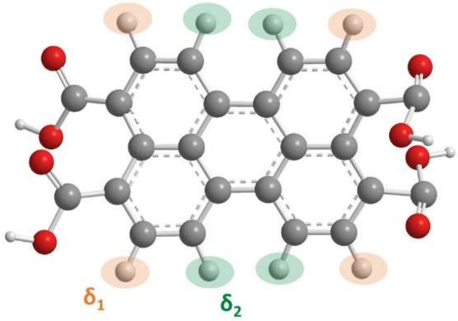

Figure S10 | Chemical shifts showing two distinct environments for the protons (δ_1 orange & δ_2 green) marked in the molecular structure.

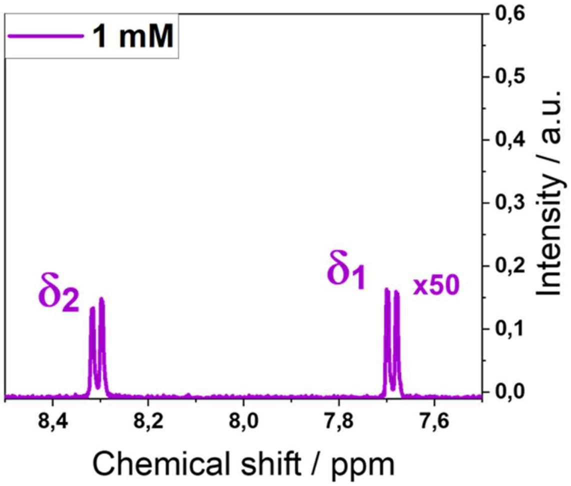

Figure S11 | 1H-NMR spectra of 1 mM PTC showing the distinct proton resonances (δ_1, δ_2).

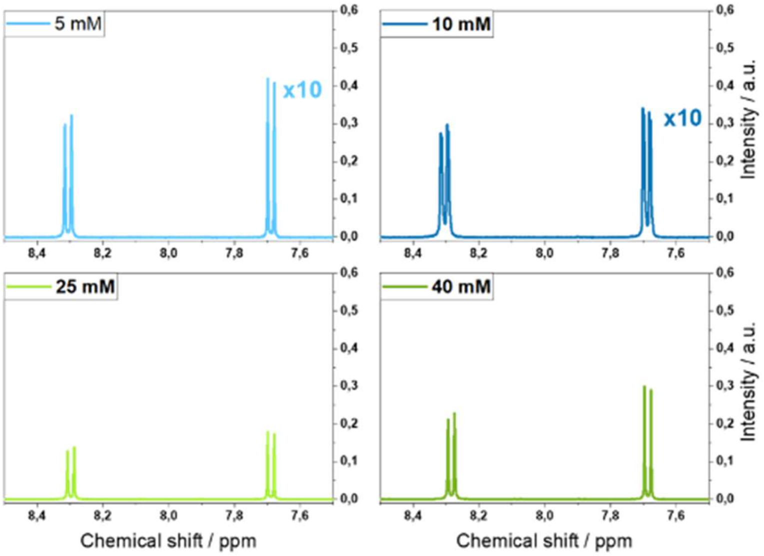

Figure S12| 1H-NMR spectra showing chemical shift of 5, 10, 25 and 40mM concentrations of PTC.

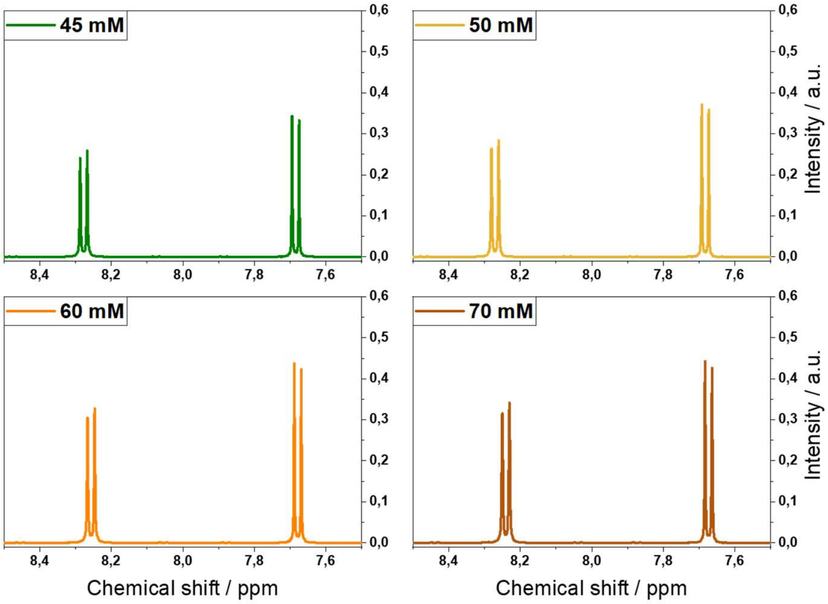

Figure S13| 1H-NMR spectra showing chemical shift of 45, 50, 60 and 70mM concentrations of PTC.

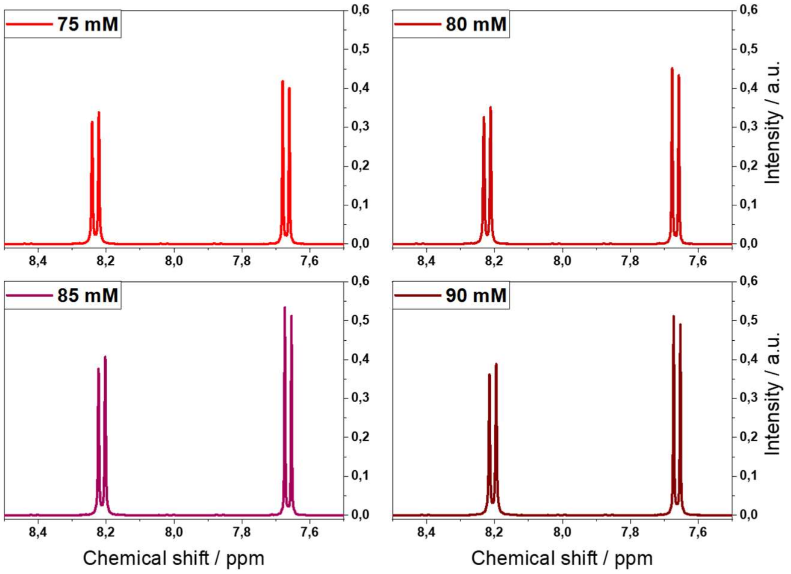

Figure S14 | 1H-NMR spectra showing chemical shift of 75, 80, 85 and 90mM concentrations of PTC.

Table S3. Chemical shifts (δ_1, δ_2) and coupling constants (J_2) for PTC at all concentrations studied.

Concentration (mM)	Delta 1 (δ_1)	Delta 2 (δ_2)	J_2 (Hz)
90	7.8073	8.3494	7.9
85	7.8088	8.3568	7.9
80	7.8116	8.3657	7.9
75	7.8148	8.3754	7.9
70	7.8175	8.384	7.9
60	7.8227	8.4002	7.9
50	7.8264	8.4138	7.9
45	7.8294	8.4217	7.9
40	7.8299	8.4272	7.9
25	7.8324	8.4404	7.9
10	7.8348	8.4495	7.9
5	7.8319	8.4485	7.9
1	7.8333	8.4516	8.0

8.2. Modelling of PTC association

We consider three possible models of aggregation, the indefinite oligomer model which has been previously observed for perylenes in organic solvents, the dimer model and the modified dimer model where each monomer first coordinates with two potassium ions before dimerizing.

Model 1: Dimers

This is one of the simplest aggregation models and is described by:

$$P + P \overset{Q_1}{\leftrightarrow} P_2 \qquad \text{(eq. S4)}$$

The predicted chemical shift within the model immediately shifts as concentration increases (see main text) and eventually saturates, which is opposite to the observed behavior of a plateau at low concentrations followed by a pronounced shift.

Model 2: formation of oligomers

The indefinite oligomer assumes an equilibrium of the form

$$P + P \overset{K}{\leftrightarrow} P_2 + P \overset{K}{\leftrightarrow} P_3 + P \overset{K}{\leftrightarrow} P_4 + P \overset{K}{\leftrightarrow} P_5 + P \ldots \qquad \text{(eq. S5)}$$

Where we assume that the equilibrium constant K for the species with one more molecule in the oligomer is independent of oligomer size. The oligomer model requires us to choose a cut-off number of molecules, N_{max}, for the largest oligomer. Previous studies of perylene use a cut-off maximum of N_{max}=5. To verify the dependence on the size of the largest oligomer, we carry out fits with N_{max}=5, 10 and 15 molecules shown in Figure S15, S16 and 17 and done independently from the diffusion data.

The fractional population of an oligomer of size *i* can be calculated as

$$f_i = \frac{{A_0}^{i-1} K^{i-1}}{(KA_0+1)^i} \qquad \textit{(eq. S6)}$$

Where A_0 is the PTC concentration and *K* an association constant between the n-th and (n+1)-th oligomer, which we assume is independent of oligomer size (Wang, Han et al. 2003).

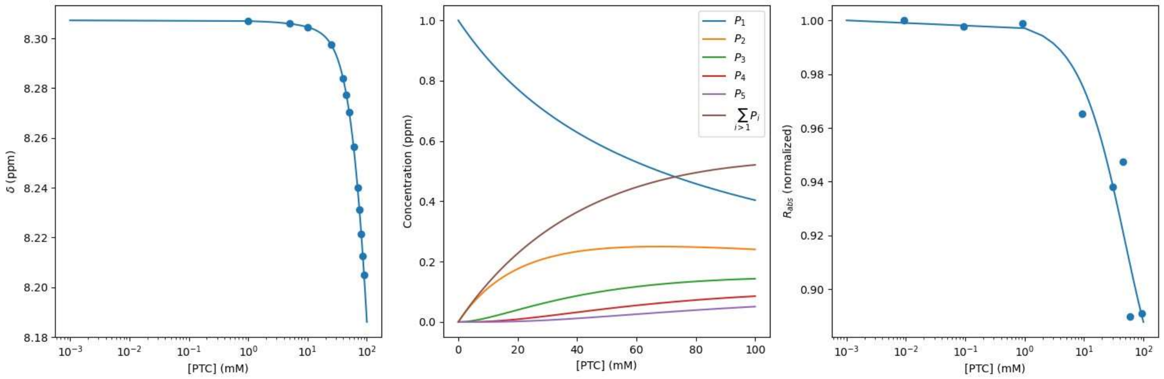

Figure S15 | Chemical shift as a function of concentration and fit using the oligomer model with cutoff Nmax=5 (left panel). Evolution of fractional oligomer populations as a function of concentration (center panel). Fit to R_{abs} using the fractional populations obtained from NMR (right panel).

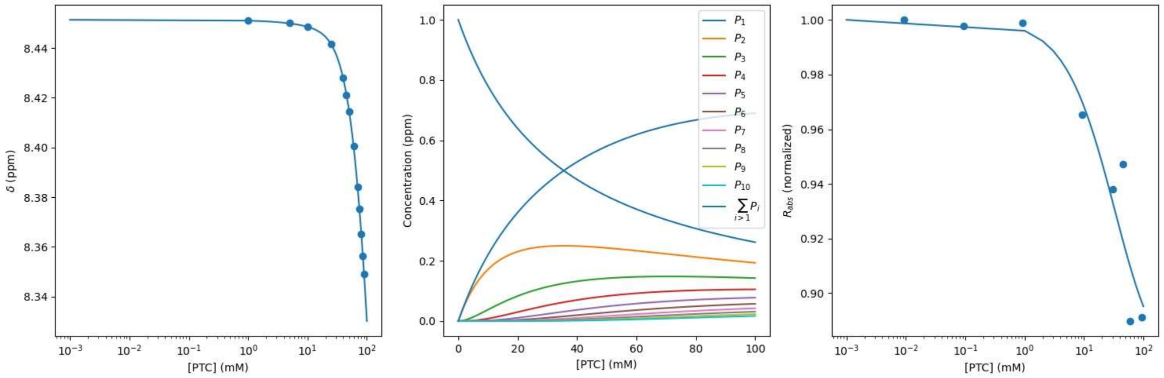

Figure S16 | Chemical shift as a function of concentration and fit using the oligomer model with cutoff Nmax=10 (left panel). Evolution of fractional oligomer populations as a function of concentration (center panel). Fit to R_{abs} using the fractional populations obtained from NMR (right panel).

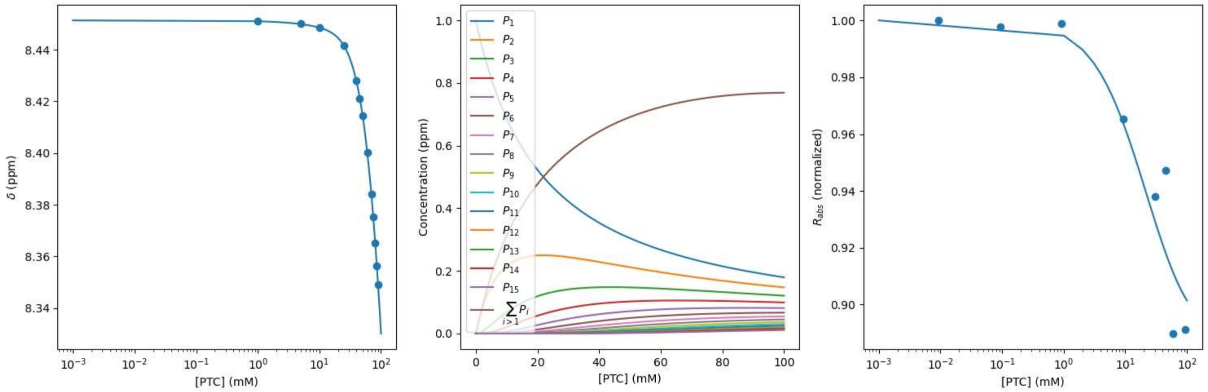

Figure S17 | Chemical shift as a function of concentration and fit using the oligomer model with cutoff Nmax=15 (left panel). Evolution of fractional oligomer populations as a function of concentration (center panel). Fit to R_{abs} using the fractional populations obtained from NMR (right panel).

Table S4. Fit parameters for oligomers with different Nmax.

Nmax	K (M-1)	g (cm-1)	% monomer at 100 mM
5	14.76	172	40
10	28.19	122	26
15	45.67	102	18

The quality of the fit remains unsurprisingly excellent as we add more parameters. Since we cannot determine independently the chemical shift of oligomers of different sizes, the maximum size cut-off cannot be determined from the chemical shift dependence alone. We observe that the aggregation constant K increases with oligomer size to reach 45.7 M^{-1} for N_{max}=15 while monomer fractional population at 100 mM decreases with increasing N_{max} and reaches 18%. The electronic coupling constant decreases to 102 cm^{-1}. However, the fit never converges as we increase N_{max} which we would expect. Global fit with the diffusion data does not improve the fit.

Model 3: Modified dimers

We further investigate alternate models to the indefinite aggregation that could explain the chemical shift dependence. A signature of the NMR chemical shift dependence is that the upfield shift does not happen at low concentrations but is delayed until after 10 mM. The standard dimer model in dynamic equilibrium cannot explain this delayed onset of the shift. We thus consider the formation of dimers with intermediate gating steps that we take to be the coordination of PTC with K$^+$ ions. The specific kinetic model is:

$$P^{|4-} + K^+ \overset{Q_1}{\leftrightarrow} PK^{|3-} \qquad \text{(eq. S7)}$$

$$PK^{|3-} + K^+ \overset{Q_2}{\leftrightarrow} {PK_2}^{|2-} \qquad \text{(eq. S8)}$$

$$ {PK_2}^{|2-} + {PK_2}^{|2-} \overset{Q_3}{\leftrightarrow} {(PK_2)_2}^{|4-} \qquad \text{(eq. S9)}$$

Where $Q_i=q_{i,forward}/q_{i,backward}$ and $q_{i,forward}$ ($q_{i,backward}$) are the forward (backward) rate constants. We allow for each of the chemical species P, PK, PK_2, $(PK_2)_2$ to have distinct chemical shifts, and calculate the observed chemical shift in the fast exchange limit as weighted average

$$\delta_{observed} = f_P\delta_P + f_{PK}\delta_{PK} + f_{PK_2}\delta_{PK_2} + f_{(PK_2)_2}\delta_{(PK_2)_2} \qquad \text{(eq. S10)}$$

where f_i are the fractional populations for the *i*-th species. The fits for the model, the fractional populations as a function of PTC concentration is shown in log scale for concentration in figure 5 of the manuscript and in lineal scale for concentration in figure S18.

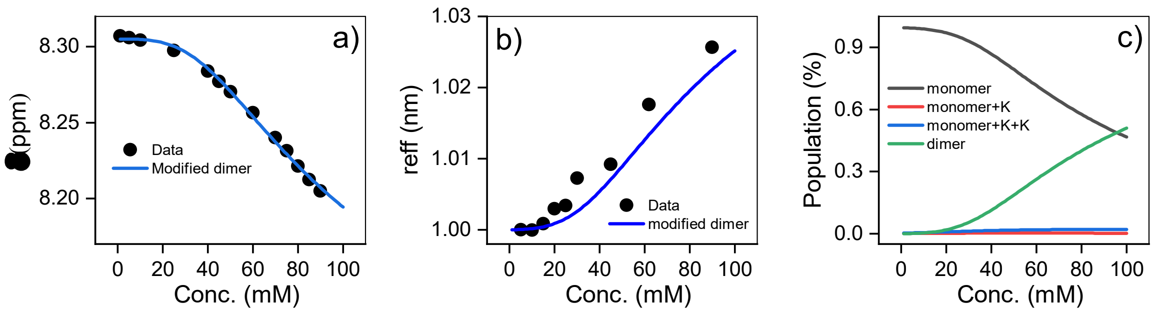

Figure S18 | a) 1H NMR chemical shift of PTC as a function of concentration, along with the fit to modified dimer model. b) Effective radius extracted from DOSY measurements fit with modified dimer model. c) Species populations for the modified dimer model.

8.3. DOSY experiments

The samples were prepared in deuterated water (D2O, 99.96%-d, Eurisotop) containing 100 µM sodium 3-(trimethylsilyl)propionate (d4-TMSP) as an internal reference; 54 mM, 39 mM, 31 mM, 22.3 mM, 18 mM, 13.3 mM, 9 mM and 4.6 mM solutions of PTC were obtained by dilution of a freshly prepared stock solution of PTC (80 mM, in 0.5M KOH) in 0.1 M KOH. The accurate concentration of each samples were determined by quantitative 1H NMR measurements using sucrose solutions of known concentrations in deuterated water, as standards, and the ERETIC2 module to analyze the data. For the measurements, 600 µL of each solution was used.

NMR spectra were recorded on a Bruker Avance spectrometer operating at 500.18 MHz for 1H, equipped with a 5 mm z-gradient BBI probe. All measurements were performed at 298 K. Chemical shifts were reported to the TMSP signal fixed at 0.00 ppm. In pulsed field gradient 1H NMR mode, the diffusion-filtered spectra were recorded with the standard stimulated echo bipolar pulse gradient sequence (stebpgp1s). The amplitude of the trapezoidal gradient pulses (g) varying from 0.02 to 0.43 T/m. The diffusion coefficients were determined according to the Stejskal−Tanner equation:

$$\frac{I}{I_0} = exp(-(\gamma_H g\delta)^2 D(\Delta - \frac{\delta}{3} - \frac{\tau}{2}) \quad \text{(eq. 11)}$$

where I is the echo intensity at g and I0 is the echo intensity extrapolated to zero gradient, γH is the 1H gyromagnetic ratio, D is the self-diffusion coefficient of the species considered, δ are gradient pulse duration, Δ delay during which the diffusion is observed, and τ is the time interval between the bipolar gradient pulses. The experiments were carried out with δ/2 = 1 ms, Δ = 100 ms, and τ = 0.2 ms. The recycle delay was 14 s. Bruker Topspin software package was used for processing all spectra.

In each sample, the experimentally determined diffusion coefficient (D) was corrected by the variation of the intrinsic viscosity of the medium, estimated by measuring the diffusion coefficient of the residual TMSP.

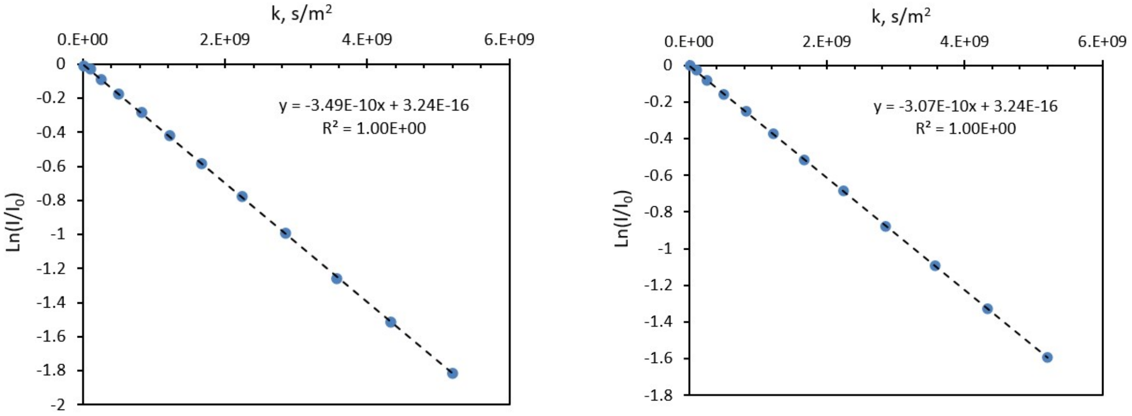

Figure S19 | Logarithmic plots of the signal attenuation for the CH resonance at ~8.4 ppm (k = (γH g δ)2(Δ − δ/3 − τ/2); for the sample containing 5 mM of PTC ($D_{measured}$ = 3.49 x 10-10 m^{2}s^{-1}, left), and for the sample containing 90 mM of PTC ($D_{measured}$ = 3.07 x 10-10 m^{2}s^{-1}, right).

Table S5. Diffusion coefficients determined experimentally for PTC ($D_{PTC\ meas}$) and TMSP ($D_{TMSP\ meas}$) for solutions of increasing concentrations of PTC in aqueous KOH solutions containing 0.1 mM TMSP, and corrected diffusion coefficient of PTC accounting for the variation of the intrinsic viscosity of the samples as determined form the evolution of D_{TMSP}.

Sample	$D_{PTC\ meas}$ (m^2s^{-1}) [a]	$D_{TMSP\ meas}$ (m^2s^{-1}) [b]	$D_{TMSP}/D_{TMSP\ 0}$	$D_{PTC\ corr}$ (m^2s^{-1})
4.6 mM	3.49(2) x 10^{-10}	5.500 x 10^{-10}	1.000	3.49(2) x 10^{-10}
9 mM	3.46(4) x 10^{-10}	5.460 x 10^{-10}	1.007	3.48(8) x 10^{-10}
13.3 mM	3.43(1) x 10^{-10}	5.390 x 10^{-10}	1.020	3.50(0) x 10^{-10}
18 mM	3.40(6) x 10^{-10}	5.380 x 10^{-10}	1.022	3.48(1) x 10^{-10}
22.3 mM	3.35(6) x 10^{-10}	5.299 x 10^{-10}	1.038	3.48(4) x 10^{-10}
31 mM	3.31(4) x 10^{-10}	5.254 x 10^{-10}	1.047	3.47(0) x 10^{-10}
39 mM	3.27(1) x 10^{-10}	5.241 x 10^{-10}	1.049	3.43(1) x 10^{-10}
54 mM	3.18(8) x 10^{-10}	5.160 x 10^{-10}	1.066	3.39(8) x 10^{-10}
80 mM	3.04(0) x 10^{-10}	4.975 x 10^{-10}	1.105	3.35(9) x 10^{-10}

[a] determined from the two aromatic signals of PTC, [b] determined from the TMSP signal fixed at 0 ppm.

Size estimation using HYDROPRO

Diffusion coefficients were estimated using HYDROPRO (Ortega, Amorós et al. 2011), from which we were able to calculate $r_{dimer}/r_{monomer}$ = 1.05. This was used to predict the effective relative radius q as

$$q = f_{monomer} + f_{dimer}\frac{r_{dimer}}{r_{monomer}} \qquad \text{(eq. 12)}$$

for the modified dimer model.

The structures for trimers and higher aggregates that are used in the oligomer model cannot be optimized with DFT as the binding is too weak. We make a simplifying assumption which should work as a lower bound model

$$q = f_{monomer} + f_{dimer}(1+\Delta) + f_{trimer}(1+2\Delta) + \cdots \qquad \text{(eq. 13)}$$

where we have defined the relative size fractional increase $\Delta = r_{dimer}/r_{monomer} - 1$.

9. Molecular Simulations

9.1. Monomer Conformations

We determined the predominant monomer charge configuration through the following approach. Various monomers were optimized with singlet multiplicity by adjusting the total charge (-4, -3, -2, and -1; Figure S19). We then calculated absorption spectra and compared them with the 3 bands identified in the experiments (466, 457, and 414 nm). Table S6 compares the absorption wavelengths calculated for each charged species with the experimental data. This comparison reveals that the monomer with a charge of -2 and hydrogens on opposite sides of the molecule is the best match to experiment. We next observed the structural behavior of this -2 monomer in the presence of bulk water by *ab initio* molecular dynamics (AIMD). One system with monomer concentration 0.26 mol/l was generated and simulated for 30 ps in a cubic simulation box (edge length: 24.312 Å; see Fig. S21) filled with 432 water molecules (for more details on the AIMD set-up see method section in the MT). The protonation state of the monomer remained stable throughout the equilibrated AIMD trajectory (17 ps). The carboxylic and carboxylate groups are found systematically involved in strong H-bond interactions with water molecules, whereas we do not observe the formation of intramolecular carboxylate-carboxylic H-bonds during the trajectory.

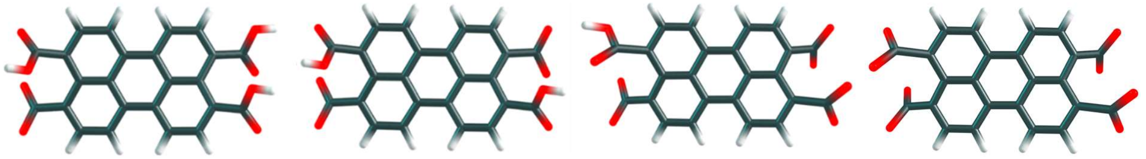

Figure S20| From left to right, geometry of the most stable tetra-substituted perylene conformer with -1, -2, -3 and -4 net charge. The geometries have been calculated with a PCM model in water at the M06/6-31g theory level.

The carboxylic O-H bonds are seen to be highly reactive in proton transfer mechanisms to water molecules and/or carboxylate groups in their proximity. This phenomenon can be appreciated in Fig. S21, where a proton transfer from a carboxylic to a carboxylate group, mediated by three water molecules, is described by the temporal evolution of the O-H bond distances of both groups. The reaction mechanism is characterized by a decrease in the O-H1 distance (black curve in Fig. S22) and a simultaneous increase in the O-H2 distance (red curve in Fig. S22).

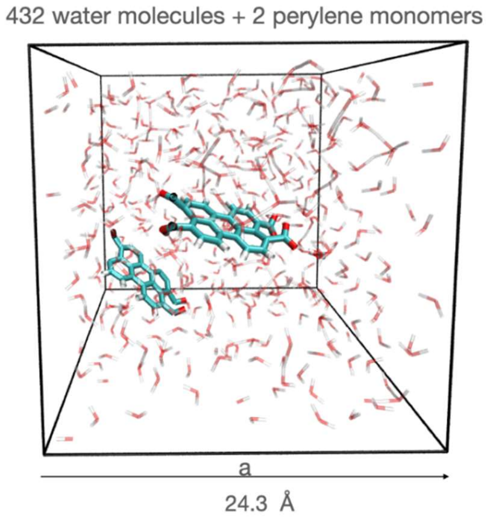

Figure S21| Boxes adopted for the simulation of the perylene monomers by AIMD. The system has a monomer concentration of 0.26 mol/l. The hydrogen atoms are depicted in white, the oxygens in red and the carbons in light blue.

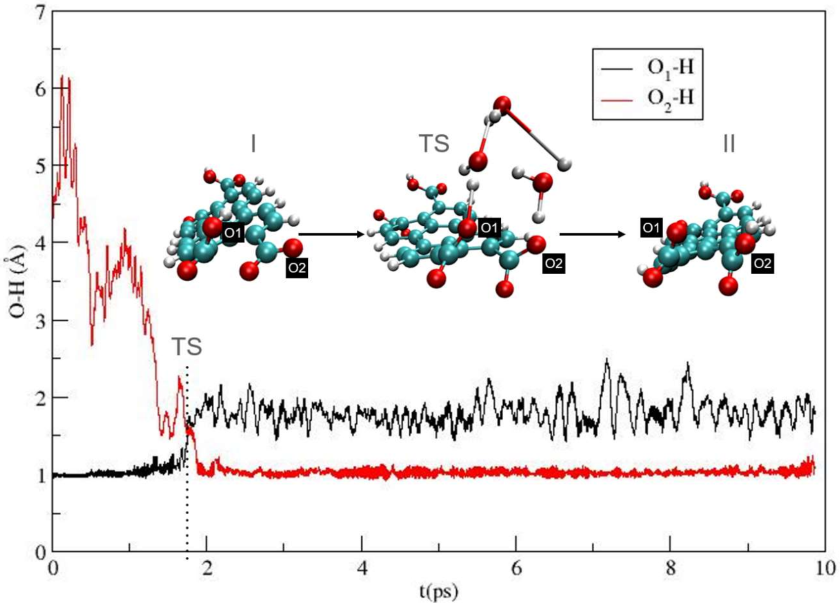

Figure S22| Temporal evolution of the carboxylic OH bonds (O1-H and O2-H) involved in the proton transfer mechanism between the carboxylic and carboxylate groups observed along the dynamics. The evolution of the O1-H and the O2-H distances in time is represented by the black and red curves, respectively; the instant of the transition is highlighted by a dashed black curve. A scheme of the reaction is shown above the traces, going from the reactant (I) to the product (II). The carbon, hydrogen and oxygen atoms are represented in blue, red and white spheres, respectively.

Table S6| Absorption bands for different protonation states at the M06/6-31G level with PCM model in water. For twice deprotonated geometries, a) refers to those with each hydrogen located at each end of the molecule and b) for the hydrogens positioned on the same side of the molecule.

Experimental (nm)	Charge=-4	Charge=-3	Charge=-2 (a)	Charge=-2 (b)	Charge=-1
414		402	433	~444	417
457		435	~479	483-493	469
466	482	491	483	~529	486

9.2. Dimer Conformation

Structural optimization of dimers, and calculations of their vibrational frequencies and excited states, were carried out using the Gaussian 16 software (Frisch, Trucks et al. 2019). All calculations were performed with a solvent model (PCM), using a dielectric constant of 78.35 to simulate the aqueous solvent (Tomasi and Persico 1994). The configurational search for dimers was performed by placing the monomers (with a charge of -2; see above) in the center of cubic boxes of various lengths and allowing them to evolve under annealing conditions, according to the internals of the ASCEC program (Pérez and Restrepo 2008, Pérez, Florez et al. 2008, Pérez, Hadad et al. 2008). The geometric characterization is performed in terms of twist and tilt angles as defined in Figure S23.

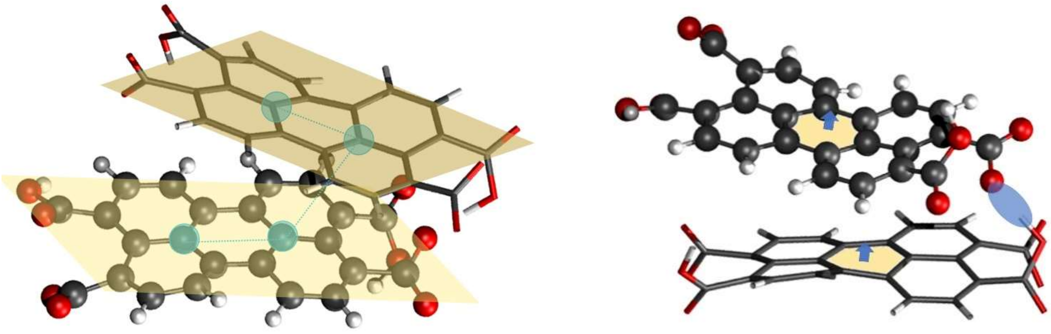

Figure S23. Schematic representation of the dimer twist and tilt angles considered. Left: The twist angle is defined as the dihedral angle formed from the three consecutive vectors connecting the four carbon atoms which are represented as blue spheres Right: The tilt angle is defined as the angle between the two vectors perpendicular to the central C6 units of each monomer.

After the generation of candidate structures to be minima on the potential energy surface, these structures were subsequently optimized and classified as true minima by evaluating the eigenvalues of the Hessian matrix at the DFT theory level, using the functional M06 and the base 6-31g. The M06 functional was adopted because it has shown the best performance in reproducing the experimental absorption spectra of the perylene dimers (see section below for the benchmark). In Figure S27, we can see the relative energies and geometries of the 10 lowest energy dimers found with overall charge -4. The initial ten minima exhibit two distinct shapes: square types $SD1_{-4}$ -$SD6_{-4}$ and cross types $SD7_{-4}$-$SD10_{-4}$.

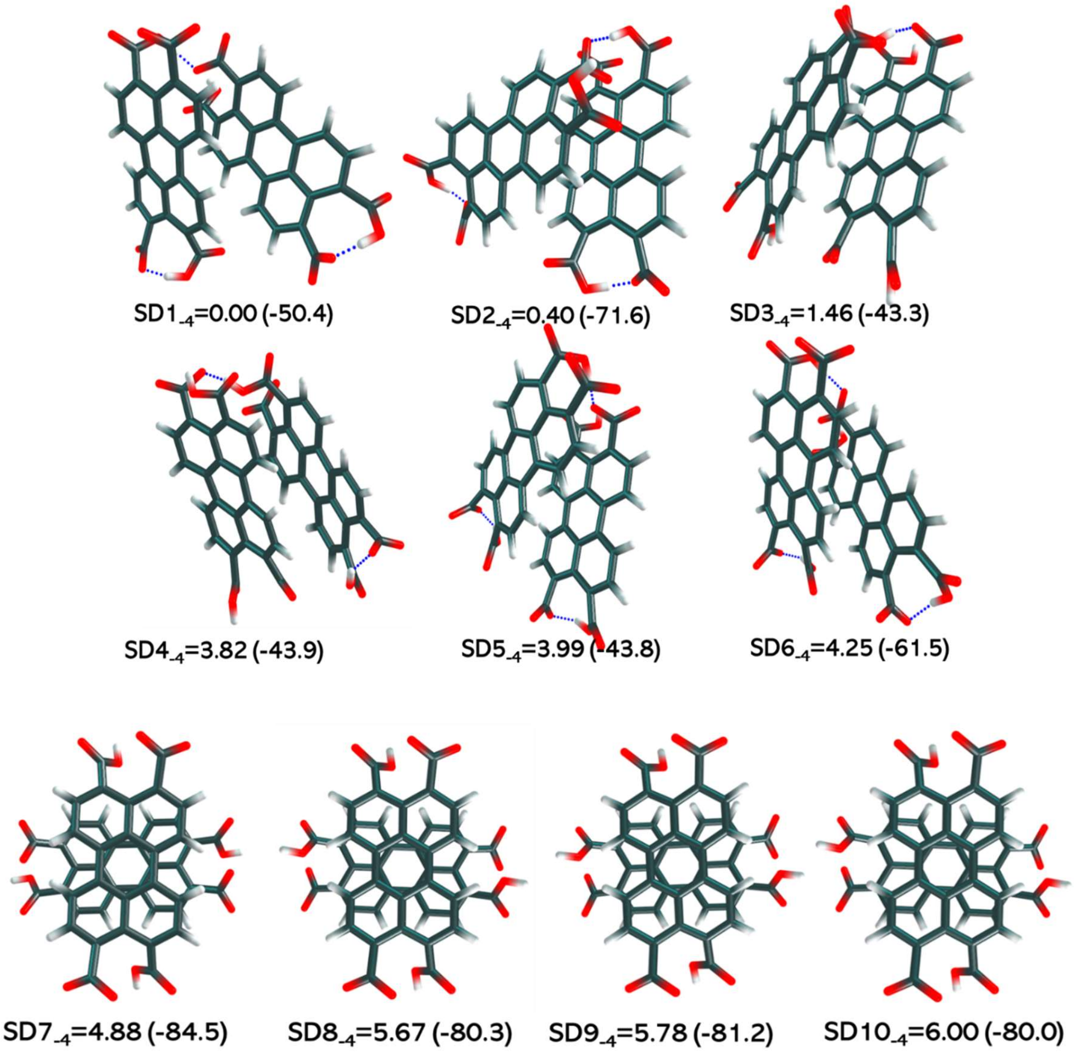

$SD1_{-4}$=0.00 (-50.4) $SD2_{-4}$=0.40 (-71.6) $SD3_{-4}$=1.46 (-43.3)

$SD4_{-4}$=3.82 (-43.9) $SD5_{-4}$=3.99 (-43.8) $SD6_{-4}$=4.25 (-61.5)

$SD7_{-4}$=4.88 (-84.5) $SD8_{-4}$=5.67 (-80.3) $SD9_{-4}$=5.78 (-81.2) $SD10_{-4}$=6.00 (-80.0)

Figure S24. The first ten minima for dimers with charge -4 (relative energy indicated in kcal/mol; twist angle in parenthesis). The definition of the twist angle is shown in Figure S23. The geometries have two distinct shapes: square types SD1-4 to SD6-4 and cross types SD7-4 to SD10-4. We can identify square-type minima by observing intermolecular hydrogen bonds between both monomers. Calculations were performed using the M06/6-31g theory level and a PCM model to simulate the aqueous solvent

The different characteristics of the dimers are summarized in Table S7. Square-type minima are identified by the presence of intermolecular hydrogen bonds between both monomers, which explains their higher stability. These square minima can be further categorized into two subtypes: i) hydrogen bonds formed with the oxygen atoms at the edges of the carbonyl group (minima $SD2_{-4}$ and $SD6_{\_4}$), with dihedral angles ranging from -61.5 to -71.6. ii) Hydrogen bonds established with the inner oxygen atoms of the carbonyl group (minima $SD1_{-4}$, $SD3_{-4}$, $SD4_{-4}$, and $SD5_{-4}$), accompanied by dihedral angles spanning from -43.3 to -50.4. Another significant distinguishing characteristic of this initial group of compounds is the presence of intramolecular hydrogen bonding. Specifically, structures $SD1_{-4}$, $SD2_{-4}$, $SD5_{-4}$, and $SD6_{-4}$ exhibit two intramolecular hydrogen bonds, geometry $SD4_{-4}$ features only one, and geometry $SD3_{-4}$ lacks any intramolecular hydrogen bonds. In contrast, the cross-type structures (minima $SD7_{-4}$-$SD10_{-4}$), stabilized by π-stacking, primarily differ in their dihedral angles, which vary from -80.0 to -84.5.

Table S7. Relative energy in kcal/mol, adjusted with the zero-point energy, for the most energetically favorable -4 charged dimers. Calculations were performed using the M06/6-31g theory level and a PCM model to simulate the aqueous solvent

Configuration	Relative energy (kcal/mol)	Dihedral	Shape
SD1	0.00	-50.4	Square
SD2	0.40	-71.6	Square
SD3	1.46	-43.3	Square
SD4	3.82	-43.9	Square
SD5	3.99	-43.8	Square
SD6	4.25	-61.5	Square
SD7	4.88	-84.5	Cross
SD8	5.67	-80.3	Cross
SD9	5.78	-81.2	Cross
SD10	6.00	-80.0	Cross

9.3. Assessing the performance of M06 functional

In order to choose the best method to describe our system, we benchmarked it against the experimental absorption spectrum of the monomer. In Table S8, we present a comparison of the theoretical absorption spectra and associated frequencies obtained using three different functionals (CAM-B3LYP, wB97xd, and M06) against the experimental spectrum. While all three functionals reproduce the 3 bands, the oscillator strengths associated with them differ considerably. For CAM-B3LYP, the lowest-wavelength band is nearly invisible. Furthermore, the absorption wavelengths are significantly blue shifted for the CAM-B3LYP and wb97xd functionals. In contrast, M06 predicts bands at longer wavelengths that are closer to experimental values and maintain the expected relationship between them. Interestingly, we observed that the impact of the counterion on the spectrum is minimal; its main effect lies in slightly enhancing the band intensity relationship, particularly noticeable for the M06/6-31g-calculated spectrum. Hence, the M06/6-31g theory level was chosen as the most suitable for describing the system.

Table S8. Absorption bands observed in water for the most stable -4 charged dimer, along with a 4K+-like counterion, are presented across various theory levels and the 6-31g basis set with a PCM model.

Experimental (nm)	M06 (-4)	f	M06 ($4K^+$)	f	CAM-B3LYP (-4)	f	CAM-B3LYP ($4K^+$)	f	wb97xd (-4)	f	wb97xd ($4K^+$)	f
414	462	0.18	462	0.29	379	0.01	378	0.01	379	0.09	383	0.15
457	472	0.70	472	0.64	406	1.16	407	1.25	398	1.00	400	1.02
466	492	0.09	494	0.11	421	0.14	423	0.14	414	0.14	415	0.13

9.4. Discussion on S_1 and T_1 energies for the PTC monomer

We discuss here the excitation energies of the first excited singlet (S_1) and triplet (T_1) states for the PTC monomer. The energy of S_1 must be equal to or higher than twice the energy of T_1 for singlet fission to be possible. To evaluate this condition we compare the excitation energies of S_1 and T_1 obtained within time-dependent density functional theory (TD-DFT). We use the exchange-correlation functional M06 (Zhao and Truhlar 2008), which exhibits good performance for simulating the absorption bands for the PTC monomer, and the exchange-correlation functional CAM-B3LYP

(Yanai, Tew et al. 2004), which outperforms M06 in predicting singlet-triplet excitation energies (Jacquemin, Perpète et al. 2010). We use the basis set 6-31G and 6-311G(d,p) (Binkley, Pople et al. 1980), and a PCM model to simulate the effect of the solvent. We carry out all the TD-DFT calculations with the Q-CHEM program (Epifanovsky, Gilbert et al. 2021).

We show in Table S9 the simulated excitation energies for S_1 and T_1 for the molecular dianion of PTC in water. The functional M06 predicts that the SF process is slightly uphill ($E(S_1) < 2E(T1)$), but the energies obtained with the functional CAM-B3LYP indicate that SF might happen spontaneously ($E(S1) > 2E(T1)$). These results suggest that a spontaneous SF is feasible for the PTC dianion, but the balance between the energies of T_1 and S_1 is very sensitive to the quality of the DFT exchange-correlation functional. The assessment of the impact of the theory level, solvent, charge and molecular conformation on the excitation energies of PTC is beyond the scope of this work.

Table S9 |Simulated Excitation energies of the S1 and T1 states for the PTC molecular dianion. Column 1: Selected density functional theory (DFT) functional and basis set. Columns 2-3: Excitation energy (in eV) of the lowest energy triplet state (T1; column 2) and the first excited singlet state (S1; column 3). Column 4: Energy difference between the energy of S1 and twice the energy of T1.

DFT functional/basis set	$E(T_1)$ (eV)	$E(S_1)$ (eV)	$E(S_1)-2E(T_1)$(eV)
M06/6-31G	1.3321	2.6198	-0.0444
M06/6-311G(d,p)	1.3259	2.5391	-0.1127
CAM-B3LYP/6-31G	1.2533	2.9460	0.4394
CAM-B3LYP/6-311G(d,p)	1.2355	2.8274	0.3564

9.5. Evolution of excitation energies and electronic couplings with the time

In order to evaluate the excitation energies of the states involved in the SF process and the electronic (interstate) couplings that determine the SF rate, we use an excitonic model which consists of five diabatic states: two low-lying local excited states (LE), two low-lying charge-transfer states (CT), and the correlated triplet pair state $^1(TT)$ (Carreras, Uranga-Barandiaran et al. 2019). To label these diabatic states we use the subindexes 1 and 2 to refer to each of the monomers of PTC in the selected dimer configurations (see Figure S25). Monomers 1 and 2 are not equivalent, as they interact through a hydrogen bond between the carboxyl group (R-COOH) of one monomer and the carboxylate group ($R-COO^-$) of the other. In most of the selected configurations, monomer 1 donates the proton (hydrogen bond donor) to monomer 2 (hydrogen bond acceptor) but for some configurations, the situation is reversed and monomer 1 is the hydrogen bond acceptor and monomer 2 is the hydrogen bond donor.

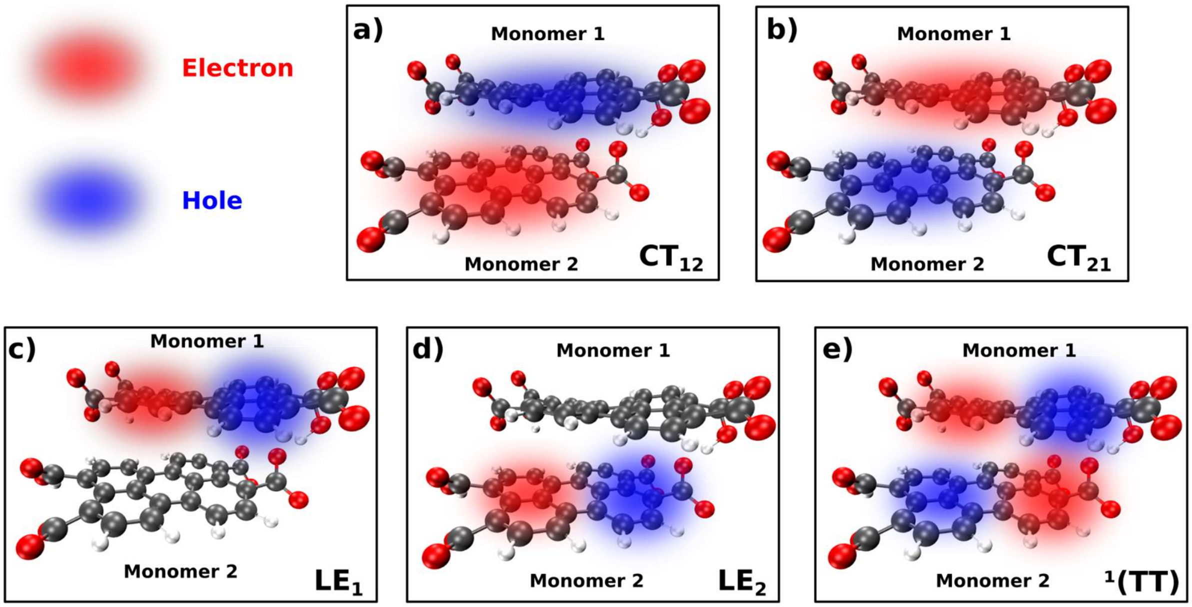

Figure S25 | Sketch of the electron distribution in the diabatic states that define the excitonic model for the PTC dimer. The red and blue areas represent regions of electron density accumulation (electron) and depletion (hole), respectively. (a) Charge-transfer state from monomer 1 to monomer 2 (CT12). (b) Charge-transfer state from monomer 2 to monomer 1 (CT21). (c) Local excited state localized to monomer 1 (LE1). (d) Local excited state localized to monomer 2 (LE2). (e) Correlated triplet-pair state ^{1}(TT). The spheres colored white, grey and red represent the atoms of hydrogen, carbon and oxygen, respectively.

We show in Tables S9 and S10 the excitation energies of the lowest energy diabatic states (Table S9) and the electronic couplings (Table S10) between the selected states computed at the RASCI(4,4)HP/6-311G(d,p)(Binkley, Pople et al. 1980, Casanova 2022) (see Experimental Section in the main text for further details on the methodology) for eighteen structures of the PCT dimer selected from the AIMD simulation. We analyze the last 17 picoseconds of the AIMD simulation and select one structure per picosecond of the simulation. We use the data in Tables S9 to generate Figures 7a-b and Table S10 to generate Figures 7c-d in the manuscript.

Table S10 | Electronic couplings (see Simulation section in the main manuscript for computational details).

Interlayer distance (ps)	Twist angle (deg)	CT-med (ev)	Exciton (ev)	Direct (ev)
439.26	37.139	6.6179E-4	0.02697	0.002
481.9	30.917	0.00395	0.07174	0.00577
464.3	32.996	0.00518	0.01814	0.0028
476.1	37.48	0.00705	0.03143	0.00367
421.1	35.686	0.01015	0.02386	0.00598
465.2	30.819	0.01295	0.05339	3.0328E-4
459.4	36.375	0.01457	0.08842	0.00437
467.3	35.267	0.01635	0.01144	0.0064
459.1	39.495	0.01638	0.02218	0.00837
445.6	41.171	0.01685	0.03734	0.00705
472.5	34.088	0.02817	0.0348	0.00619
453.7	31.756	0.04138	0.02913	0.00211
445.5	41.696	0.0414	0.01213	0.0152
446.4	44.5	0.04344	0.01207	0.0097
462.8	35.734	0.04687	0.15042	0.00417
429.9	34.395	0.11556	0.04623	0.02871
454.7	37.797	0.28509	0.06768	0.00445
461.6	39.905	0.34807	0.01926	0.006
439.26	37.139	6.6179E-4	0.02697	0.002
481.9	30.917	0.00395	0.07174	0.00577
464.3	32.996	0.00518	0.01814	0.0028
476.1	37.48	0.00705	0.03143	0.00367
421.1	35.686	0.01015	0.02386	0.00598
465.2	30.819	0.01295	0.05339	3.0328E-4
459.4	36.375	0.01457	0.08842	0.00437
467.3	35.267	0.01635	0.01144	0.0064
459.1	39.495	0.01638	0.02218	0.00837
445.6	41.171	0.01685	0.03734	0.00705
472.5	34.088	0.02817	0.0348	0.00619
453.7	31.756	0.04138	0.02913	0.00211

10. References

Binkley, J. S., J. A. Pople and W. J. Hehre (1980). "Self-consistent molecular orbital methods. 21. Small split-valence basis sets for first-row elements." Journal of the American Chemical Society **102**(3): 939-947.

Carreras, A., O. Uranga-Barandiaran, F. Castet, et al. (2019). "Photophysics of Molecular Aggregates from Excited State Diabatization." Journal of Chemical Theory and Computation **15**(4): 2320-2330.

Casanova, D. (2022). "Restricted active space configuration interaction methods for strong correlation: Recent developments." WIREs Computational Molecular Science **12**(1): e1561.

Epifanovsky, E., A. T. B. Gilbert, X. Feng, et al. (2021). "Software for the frontiers of quantum chemistry: An overview of developments in the Q-Chem 5 package." The Journal of Chemical Physics **155**(8).

Flors, C. and S. Nonell (2001). "On the Phosphorescence of 1H-Phenalen-1-one." Helvetica Chimica Acta **84**(9): 2533-2539.

Frisch, M. J., G. W. Trucks, H. B. Schlegel, et al. (2019). Gaussian 16 Rev. C.01. Wallingford, CT.

Hernández, L. I., R. Godin, J. J. Bergkamp, et al. (2013). "Spectral Characteristics and Photosensitization of TiO2 Nanoparticles in Reverse Micelles by Perylenes." The Journal of Physical Chemistry B **117**(16): 4568-4581.

Jacquemin, D., E. A. Perpète, I. Ciofini, et al. (2010). "Assessment of Functionals for TD-DFT Calculations of Singlet-Triplet Transitions." J Chem Theory Comput **6**(5): 1532-1537.

Knibbe, H., D. Rehm and A. Weller (1968). "Intermediates and Kinetics of Fluorescence Quenching by Electron Transfer." Berichte der Bunsengesellschaft für physikalische Chemie **72**(2): 257-263.

Korovina, N. V., C. H. Chang and J. C. Johnson (2020). "Spatial separation of triplet excitons drives endothermic singlet fission." Nature Chemistry **12**(4): 391-398.

Margulies, E. A., C. E. Miller, Y. Wu, et al. (2016). "Enabling singlet fission by controlling intramolecular charge transfer in π-stacked covalent terrylenediimide dimers." Nature Chemistry **8**(12): 1120-1125.

Murov, S. L., I. Carmichael and G. L. Hug (1993). Handbook of Photochemistry, Second Edition, CRC Press.

Oliveros, E., S. H. Bossmann, S. Nonell, et al. (1999). "Photochemistry of the singlet oxygen [O2(1Δg)] sensitizer perinaphthenone (phenalenone) in N,N′-dimethylacetamide and 1,4-dioxane." New Journal of Chemistry **23**(1): 85-93.

Ortega, A., D. Amorós and J. García de la Torre (2011). "Prediction of hydrodynamic and other solution properties of rigid proteins from atomic- and residue-level models." Biophys J **101**(4): 892-898.

Pérez, J. and A. Restrepo (2008). "ASCEC V–02: Annealing Simulado con Energía Cuántica." Property, development and implementation: Grupo de Química–Física Teórica, Instituto de Química, Universidad de Antioquia: Medellín, Colombia.

Pérez, J. F., E. Florez, C. Z. Hadad, et al. (2008). "Stochastic Search of the Quantum Conformational Space of Small Lithium and Bimetallic Lithium−Sodium Clusters." The Journal of Physical Chemistry A **112**(25): 5749-5755.

Pérez, J. F., C. Z. Hadad and A. Restrepo (2008). "Structural studies of the water tetramer." International Journal of Quantum Chemistry **108**(10): 1653-1659.

Tomasi, J. and M. Persico (1994). "Molecular Interactions in Solution: An Overview of Methods Based on Continuous Distributions of the Solvent." Chemical Reviews **94**(7): 2027-2094.

Walker, B. J., A. J. Musser, D. Beljonne, et al. (2013). "Singlet exciton fission in solution." Nature Chemistry **5**(12): 1019-1024.

Wang, W., J. J. Han, L.-Q. Wang, et al. (2003). "Dynamic π−π Stacked Molecular Assemblies Emit from Green to Red Colors." Nano Letters **3**(4): 455-458.

Watkins, A. R. (1974). "Kinetics of fluorescence quenching by inorganic anions." The Journal of Physical Chemistry **78**(25): 2555-2558.

Yanai, T., D. P. Tew and N. C. Handy (2004). "A new hybrid exchange–correlation functional using the Coulomb-attenuating method (CAM-B3LYP)." Chemical Physics Letters **393**(1): 51-57.

Zhao, Y. and D. G. Truhlar (2008). "The M06 suite of density functionals for main group thermochemistry, thermochemical kinetics, noncovalent interactions, excited states, and transition elements: two new functionals and systematic testing of four M06-class functionals and 12 other functionals." Theoretical Chemistry Accounts **120**(1): 215-241.